Peer-reviewed version available at Geosciences 2016, 6, 39; doi:10.3390/geosciences6030039

Article

Regional Lithological Mapping Using ASTER-TIR Data: Case Study for the Tibetan Plateau and the Surrounding Area

Yoshiki Ninomiya [1,*] and Bihong Fu [2]

[1] Geological Survey of Japan, AIST, Tsukuba 3058567, Japan
[2] Institute of Remote Sensing and Digital Earth, Chinese Academy of Sciences, Beijing 100094, China; fubh@radi.ac.cn
* Correspondence: yoshiki.ninomiya@aist.go.jp; Tel.: +81-29-861-3975

Abstract: The mineralogical indices; the Quartz Index (QI), Carbonate Index (CI) and Mafic Index (MI) for ASTER multispectral thermal infrared (TIR) data were applied to various geological materials for regional lithological mapping on the Tibetan Plateau. Many lithological and structural features are not currently well understood in the central Tibetan Plateau, including the distribution of mafic-ultramafic rocks related to the suture zones, the quartzose and carbonate sedimentary rocks accreted to the Eurasian continent, and sulfate layers related to the Tethys and neo-Tethys geological setting. These rock types can now be mapped with the interpretation of the processed ASTER TIR images described in this paper. A methodology is described for the processing of ASTER TIR data applied to a very wide region of the Tibetan Plateau. The geometrical and radiometric performance of the processed images is discussed, and the advantages of using ortho-rectified data are shown. The challenges of using ASTER data with small footprint in addition to selecting an appropriate subset of scenes are also examined. ASTER scenes possess a narrow swath width when compared to LANDSAT data (60 km vs. 185 km respectively). Furthermore, the ASTER data archive is vast consisting of approximately 3 million images. These details can present an added level of complexity during an image processing workflow. Finally, geological interpretations made on the maps of the indices are compared with prior geological field studies. The results from the investigations suggest that the indices perform well in the classification of quartzose rocks based on the carbonate and the mafic mineral content, in addition to the granitic rocks based on the feldspar content.

Keywords: ASTER; TIR; geology; mineralogy; suture zone; quartz; feldspars; silicates; carbonates; sulfates; granitic rocks; felsic; ultramafic; mapping

1. Introduction

Spectroscopic studies of inorganic materials in the thermal infrared (TIR) region (8–12 μm) [1,2] have demonstrated strong absorption features caused by the stretching vibrations of the Si–O bonds in silicate minerals, the major components of the terrestrial surface, whereas the Si–O bonds do not cause any prominent spectral features in the visible and near infrared (VNIR) region of the spectrum (0.4–2.5 μm) [3]. Studies carried out during the Apollo missions to the Moon in the 1960's, confirmed relationships between the TIR spectral features and geology of the Lunar surface composition (e.g., [4,5]). For example, it was observed that the emissivity minima due to Si–O stretching vibrations (i.e., reststrahlen bands) moved to longer wavelengths as the composition of the target igneous rocks changes from felsic to ultramafic [6].

The airborne and satellite remote sensing systems were developed after the results of the spectroscopic studies shown above. They demonstrated the capability of detecting rock composition, despite the radiometric, spectral and spatial resolutions being much worse when compared to the modern system like ASTER. For example, an airborne scanner with two detector elements could distinguish quartz sandstone from nonsilicate surface materials [7]. Additionally,

Peer-reviewed version available at Geosciences 2016, 6, 39; doi:10.3390/geosciences6030039

the infrared interferometric spectrometer onboard the Nimbus–4 satellite derived a global surface emissivity map at 9μm, which discovered the significant low emissivities over arid areas due to quartz, even with a quite low spatial resolution (~100-km) [8].

The airborne Thermal Infrared Multispectral Scanner called TIMS was the first modern thermal infrared remote sensing system with resolutions adequate for geological applications (e.g., [9,10]]. TIMS and similar airborne systems (e.g., [11]) confirmed their capabilities of detecting the systematic shift of the reststrahlen bands in the silicate rocks and minerals.

The Advanced Spaceborne Thermal Emission and Reflection Radiometer (ASTER) sensor developed by Japanese government was launched onboard Terra, the first of NASA's Earth Observing System (EOS) series of satellites, in December 1999 [12]. It is composed of three subsystems: 1) VNIR subsystem observing the visible to near-infrared region (three bands between 0.5 and 0.9-μm, 15-m resolution, region, and with a stereoscopic capability for the NIR band); 2) SWIR subsystem observing the shortwave infrared region (six bands between 1.6 and 2.5-μm, 30-m resolution); and 3) TIR subsystem observing the thermal infrared region (five bands between 8 and 12-μm, 90-m resolution, NEΔT<0.3 K at 300 K), respectively. The spatial coverage of an ASTER image at the surface is approximately 60×60 km.

The authors have proposed mineralogical indices defined with the ratioing approach of the ASTER data for detecting lithology or mineralogy [13–17]. Especially, Quartz Index (QI), Carbonate Index (CI) and Mafic Index (MI) defined for the ASTER–TIR data are finely analyzed theoretically and practically, and the performance of the indices in extracting geological information is confirmed [14]. Many studies have applied the indices (e.g., [13-19]) and other workers have proved the usefulness and stability of the indices in the local geological case studies (e.g., [20–29]). Despite ASTER radiance registered at the sensor data without atmospheric corrections applied are adopted for the calculation of the indices, the recognized scene dependency is quite weak if the atmospherically well conditioning data are selected [17].

One of the main goals of this project is the mapping of large-scale structure and lithology. We therefore commenced research for regional scale mapping covering a wide area with the spectral indices. Considering the relatively narrow spatial coverage of each ASTER data compared to that of LANDSAT, many scenes need to be mosaicked for mapping a wide area. Additionally, the ASTER data archive is vast and constantly expanding due to collection of data over the past 16 years that ASTER has been in operation. This makes it difficult to locate suitable scenes when mapping a region of interest. To save time and labor, the selection of well-conditioned data, in addition to prioritizing the selected data, and calculating the indices and mosaicking the imagery, were followed [30].

In this paper, we present the regional maps of the indices covering the region of the central Tibetan Plateau and the surrounding area, after summarizing the geology of the study area and introducing the methodology of calculating the indices and producing the regional maps. In total, 386 ASTER products are selected from a databese of more than 10,000 scenes to produce the regional maps. The characteristics of the indices for typical geological and the other materials and the radiometric and the geometrical performances of the produced maps are discussed. Finally, geological interpretations are made in association with the maps.

2. Materials and Methods

2.1. Study Area

The study area is the central part of the Tibetan Plateau and the surrounding area, bounded by latitude 28° to 37° North and longitude 84° to 90° East. The previous studies (e.g., [31,32]) have revealed that the geology of the Tibetan Plateau involves multiple terranes, suture zones containing ophiolites and ophiolitic mélanges, high–P metamorphic belts, magmatic arcs, and accretionary prism complexes that largely developed during the Paleozoic–Mesozoic.

Knowledge of the pre-Cenozoic lithospheric architecture of Tibet is critical for providing initial conditions for models of Tibetan Plateau formation, for establishing strain markers to quantify

Cenozoic deformation, and for the development of hypotheses to explain heterogeneous tectonism related to the Cenozoic Indo–Asian collision. From northeast to southwest, Tibet is comprised of the Altyn Tagh-East Kunlun-Qilian, Songpan-Ganzi, Qiangtang, Lhasa and Himalayan terranes, which are separated by east striking suture zones of Paleozoic to Mesozoic age (Figure 1). Many researchers [31,32] proposed that the formation and evolution of the Tibetan Plateau have been intrinsically related to those of the eastern Tethys, recorded by the Longmu Co–Shuanghu ophiolite mélange zone, the Southern Qiangtang Paleozoic accretionary arc-basin system, the Bangong–Nujiang suture zone, and their associated, composite island arc-basin systems. The present-day Bangong–Shuanghu–Changning–Menglian suture system marks the final closure of the Tethyan Ocean. The Indus–Tsangbo Ocean opened as a back-arc basin in response to the southward subduction of the Tethyan Ocean lithosphere in the Middle Triassic. And it closed as a result of the India–Asia collision at the end of Cretaceous, followed by the northward indention of the Indian plate that resulted in significant intra-continental deformation and plateau uplift in the Cenozoic. Cenozoic deformation mainly produced a crustal scale shear zone and décollement between the Precambrian basement and the cover sequences, regional thrust faults and folds, and strike-slip fault zones.

Figure 1 shows the tectonic setting of the Tibetan Plateau and the surrounding area, modified from the previous studies [33–35]. As shown in Figure 1, this study area is composed of the blocks of Altyn Tagh–East Kunlun–Qilian terrane, Songpan–Ganzi terrane, North Qiangtang terrane, South Qiangtang terrane, Lhasa terrane and Himalayan terrane, from north to south. The most important geological features targeted in this study include the ophiolite belts appearing at the surface along the sutures of the blocks, the quartzose and carbonite sedimentary rocks deposited as the accretion wedges associated with the subduction of the oceanic plate beneath the continental plate, the granitic rocks intruded with the island arc geological setting, and the distributions of the sulfate layers as the geological evidences of the neo-Tethys environment. The field geological studies so far (e.g., [36-43]) have revealed the distribution of the target lithological features at some limited local areas in the Tibetan Plateau. However, these terranes and suture zones are poorly characterized in central Tibet, with a >1000-km-long and up to 500-km-wide tectonic belt, where the field geological surveys have not yet accomplished well for the most part of the region because this area is remote and inaccessible (Figure 1).

The geological map at the scale of 1:1,500,000 is published [44] for the entire Tibetan Plateau region including the study area. Larger scale geological maps are published at the limited locations, for example, the geological map of the ophiolite zone at the scale of 1:200,000 in the middle segment of the Indus–Tsangbo suture zone [45].

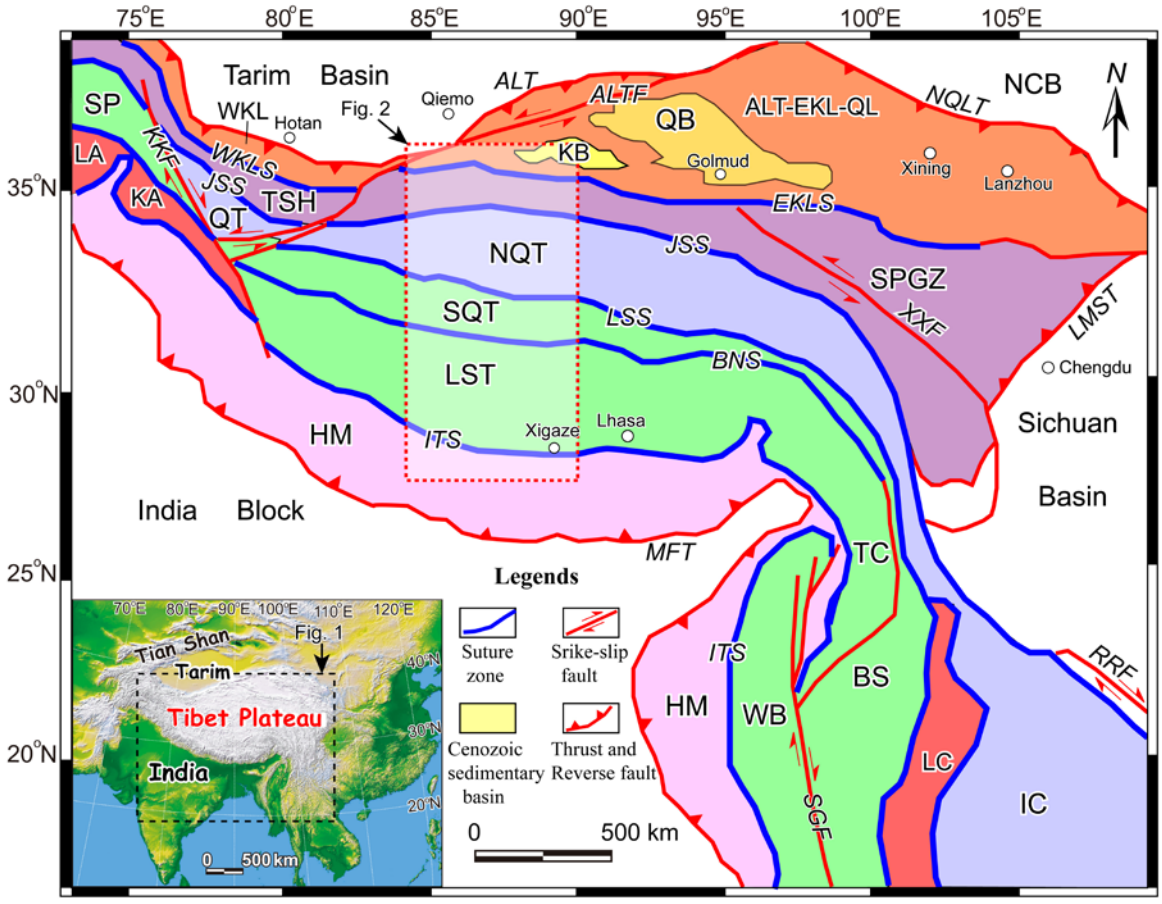

Figure 1. Simplified tectonic map of Tibet and surrounding region, showing the main suture zones in Tibet (modified from [26–28]. **Blocks and terranes:** ALT-EKL-QL: Altyn Tagh-East Kunlun-Qilian terrane; BS: Baoshan terrane; HM: Himalayan terrane; IC: Indo-China block; KA: Kohistan Arc terrane; LA: Ladakh arc terrane; LC: Lincang–Sukhothai–Chanthaburi Arc terrane; LST: Lhasa terrane; NCB: North China Block; NQT: North Qiangtang terrane; QT: Qiangtang terrane; SP: South Pamir terrane; SPGZ: Songpan-Ganze terrane; SQT: South Qiangtang terrane; TC: Tengchong terrane; TSH: Tianshuihai terrane; WB: West Burma terrane; WKL: West Kunlun terrane. **Suture zones:** BNS: Bangong-Nujiang Suture; EKLS: East Kunlun Suture; ITS: Indus-Tsangbo Suture; JSS: Jinsha Suture; LSS: Longmu Tso-Shuanghu-Menglian-Inthanon Suture; WKLS: West Kunlun Suture. **Basins:** QB: Qaidam Basin; KB: Kumkol Basin. **Faults:** ALT: Altyn Tagh Thrust; ALTF: Altyn Tagh Fault; KKF: Karakorum Fault; LMST: Longmen Shan Thrust; MFT: Main Frontal Thrust. NQLT: North Qilian Thrust; RRF: Red River Fault; SGF: Sagaing Fault; XXF: Xianshui River-Xiaojiang Fault. The dashed red rectangle represents the study area.

2.2. ASTER Data

Since the launch of ASTER in December 1999, the VNIR and TIR subsystems have observed the earth for more than 16 years. This has far exceeded its original lifespan of 5 years. The SWIR subsystem stopped operation in 2008 due to over saturation and severe striping of the detector. Ownership of the ASTER data had been held by the Ministry of Economy, Trades and Industry (METI) of Japan and NASA, and the ASTER data were distributed by the Japan Space Systems (JSS) and the USGS Eros Data Center, respectively. It was necessary to pay a nominal fee to METI for ordering ASTER data products except for the freely distributed ASTER global digital elevation model (GDEM) products [46] until March 2016. In April 2016, a change in policy was announced [47]. As a result, all ASTER data products are available at no cost. Furthermore, the ASTER data distributor in Japan has changed from JSS to the National Institute of Advanced Industrial Science and Technology (AIST).

The data observed by the ASTER sensors (Level-0 data) are transmitted to ground stations, where the data for each scene is processed to generate the standard Level-1A data product which retains the raw data observed with the sensor. Until March 2016, the ASTER data product was generated and provided as described below. Each standard and semi-standard product of the ASTER data was generated as a Hierarchy Data Format (HDF) file. The standard Level-1B data product was generated automatically for all the Level-1A data satisfying a condition on the detected cloud coverage, as well as based on the user request, which apply the fundamental geometrical and radiometric corrections essential for the most of the geoscience applications. Each pixel data in the Level-1B is in the measure of radiance registered at the sensor [48-51]. The standard higher level Level-2B data products of physical parameters including the surface radiance data with the atmospheric corrections on the Level-1B data (Level-2B01) [52,53] and the surface emissivity data with the temperature separation processing on the TIR data of the Level-2B01 data (Level-2B04) [54] were generated on the basis of the user request. Also, the semi-standard Level-4 data product of the DEMs was generated from the along-track NIR stereo images (band 3N and 3B) with the downward- and backward-viewing telescopes [55]. The semi-standard Level-3A data product with the ortho-rectification processing had been provided by JSS, which includes the radiance registered at the sensor data equivalent to the one of the Level-1B product and the ASTER-driven DEM [56].

After April 2016, AIST supplies the ortho-rectified data products corresponding to Level-3A in the GeoTIFF files [57], and USGS supplies the data products including the ortho-rectified data of the radiance registered at the sensor (Level-1T) in the HDF files [58] freely to the public covering all over the world, additionally to the ASTER GDEM products already provided to public as described above.

This study uses the ASTER products of radiance at the sensor (e.g., Level-1B, Level-3A). The DN of ASTER-TIR band i in the Level-1B or Level-3A data is linearly related to radiance registered at the sensor ($Wm^{-2}sr^{-1}\mu m^{-1}$) by [49]

$$L_{sen}^{\ i} = coef^{i} \times (DN^{i} - 1), \quad (1)$$

where $coef^{10} = 0.006882$, $coef^{11} = 0.006780$, $coef^{12} = 0.006590$, $coef^{13} = 0.005693$, and $coef^{14} = 0.005225$.

Figure 2 shows a false color composite mosaic generated with the ASTER data used in this study annotated with typical geographical information in this study area. All images of the regional maps including Figure 2 are projected using zone 43 of the Universal Transverse Mercator (UTM). As the mosaic VNIR imaging is not the purpose of this study, only an automatic color balancing of the linear stretching in the histogram region covering "average DN ± 3×σ" was applied, except for the southern part of the study area bounded by latitude 28° to 30° North, where the color balancing is carefully achieved manually.

Preprints (www.preprints.org) | NOT PEER-REVIEWED | Posted: 9 August 2016 doi:10.20944/preprints201608.0089.v1

Peer-reviewed version available at Geosciences 2016, 6, 39; doi:10.3390/geosciences6030039

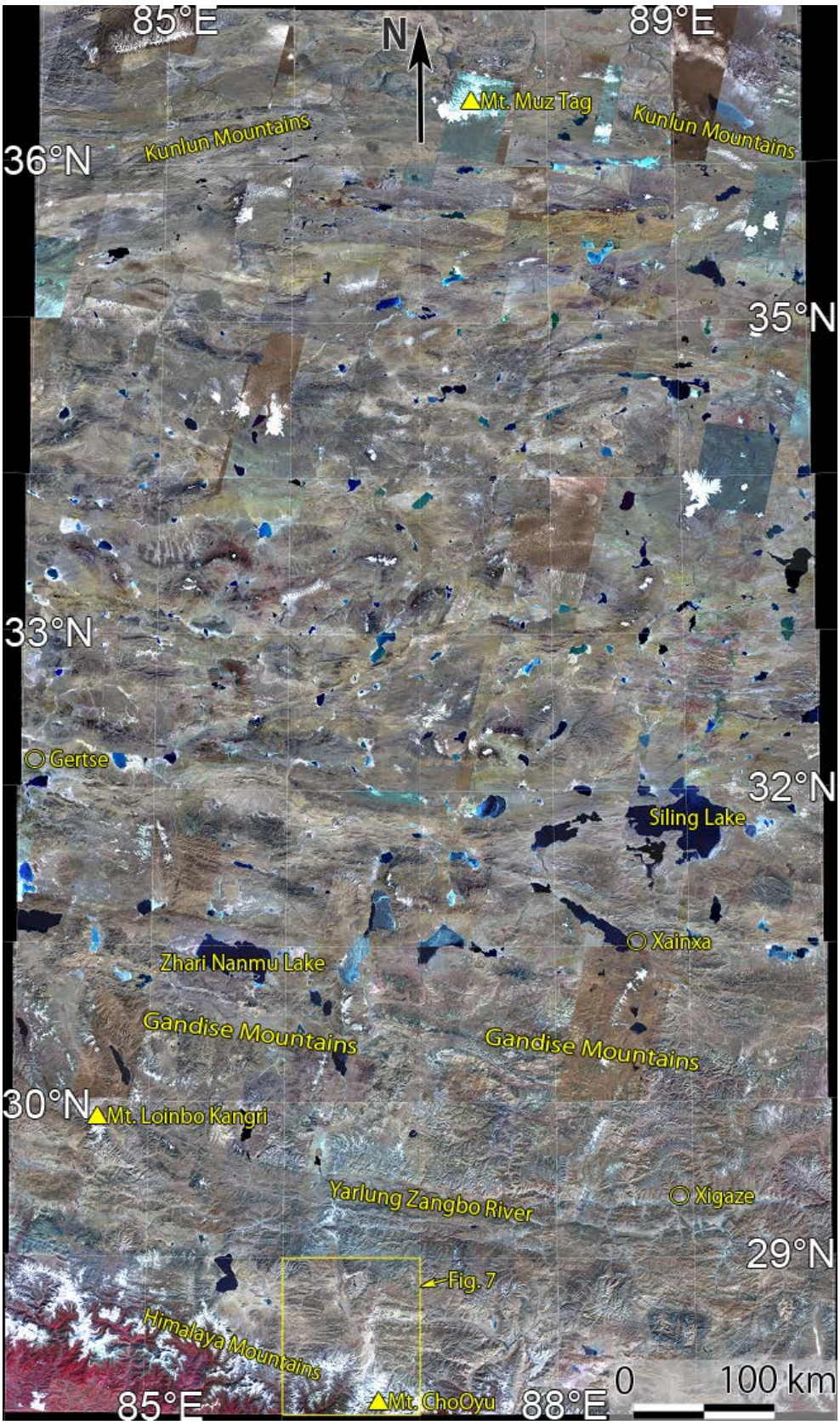

Figure 2. Mosaic VNIR false color image generated with the ASTER data used in this study, assigned blue for band 1, green for band 2 and red for band 3 covering the study area bounded by latitude 28° to 37° North and longitude 84° to 90° East, using a Universal Transverse Mercator (UTM) map projection. Geographical locations of some cities, mountains, etc. are shown. The yellow rectangle represents the area of Figure 7.

Peer-reviewed version available at Geosciences 2016, 6, 39; doi:10.3390/geosciences6030039

2.3. Mineralogical Indices for ASTER-TIR

Based on analysis of the spectral properties for typical terrestrial rocks and minerals shown in Figure 3, the indices, QI, CI and MI, were proposed [13]. After the precise analysis on the performance of the indices against the temperature and the atmospheric conditions as well as concerning the separation among the mineral types, the indices were defined [14,17] as described below.

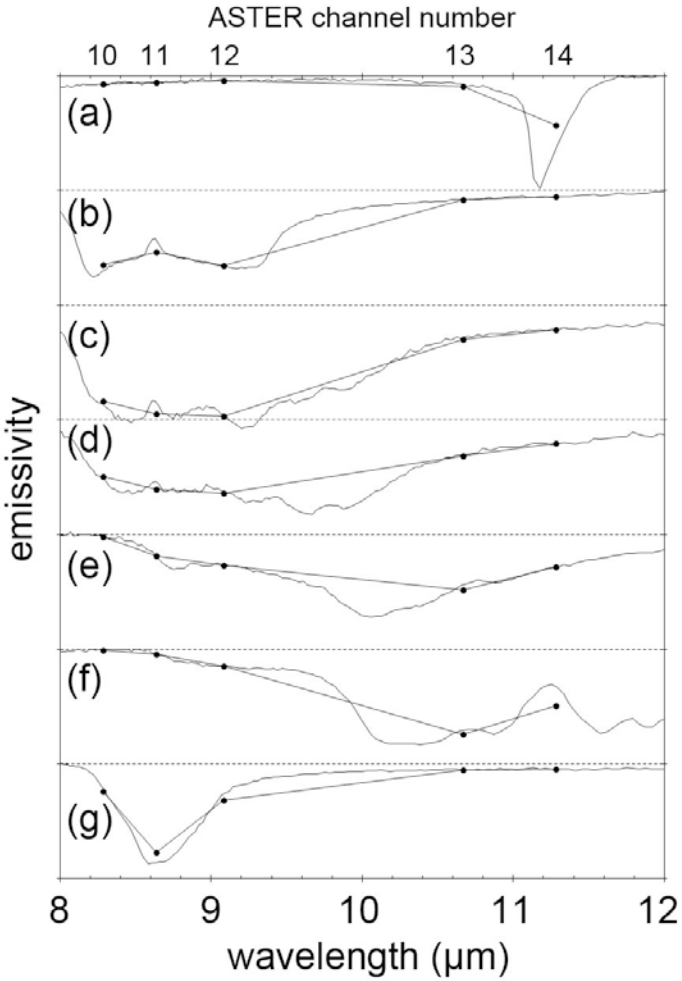

Figure 3. Emissivity spectra for common rock types (a) carbonate rock, (b) quartzose sedimentary rock, (c) felsic rock (granite), (d) intermediate rock (diorite), (e) mafic rock (gabbro), (f) ultramafic rock (dunite), (g) gypsum (modified after Ninomiya et al. [17]). Each tick in Y axis denotes 1.0 / 0.75 of emissivity except for (b) where it denotes 1.0 / 0.5 of emissivity.

To emphasize the specific spectral feature for quartz in the major rock forming minerals, e.g., higher emissivity at 8.6 μm region (corresponding to ASTER band 11) compared to the emissivity at 8.3 and 9.1μm regions (corresponding to ASTER band 10 and band 12, respectively) as shown in Figure 3 (b), QI was defined as [13]

$$QI = \frac{D_{11} \times D_{11}}{D_{10} \times D_{12}}, \quad (2)$$

where Di represents ASTER band i. In this paper, we use radiance data without atmospheric corrections of ASTER Level-1B or Level-3A data. The DN value of each pixel in Level-1B or Level-3A data is linearly converted to radiance registered at the sensor ($Wm^{-2}sr^{-1}\mu m^{-1}$) with equation (1). QI is expected to be high for crystalized quartz, on the other hand, to be low for the common sulfates typically gypsum because the spectral features for the sulfates in ASTER band 10

Peer-reviewed version available at Geosciences 2016, 6, 39; doi:10.3390/geosciences6030039

to 12 is opposite of quartz as recognized in the spectrum of gypsum shown in Figure 3 (g). Not as strong but similar as the sulfates, K-feldspars and Na-feldspars exhibit opposite spectral features of quartz. If the rocks are rich in both quartz and feldspar, which often occurs in igneous rock, typically for the granitic rocks, QI is expected to be relatively low [15,17,19,30]. The spectral emissivity property of the rock type shown in Figure 3 (c) supports this expectation. The mixture of quartz and feldspar does not generally occur in sedimentary rocks, which suggests high QI functions well as an indicator of quartz-rich sedimentary rocks. The previous studies have confirmed that high QI is a distinct indicator for quartz-rich sedimentary rocks [14-19,21-23,26,29,30], and low QI is a distinct indicator primarily of sulfate minerals [15-17,30] and secondary of feldspar-rich silicate rocks [15,17,19,30].

The spectral emissivity of carbonate rock which is composed of the two major carbonate forming minerals on Earth, calcite and dolomite, is shown in Figure 3 (a). This indicates the absorption feature is only at 11.3 μm region (corresponding to ASTER band 11), CI for ASTER TIR data was defined as [13]

$$CI = \frac{D_{13}}{D_{14}}. \tag{3}$$

CI is expected to be high for calcite and dolomite. Prior studies have confirmed that a high CI signal is a good indicator for the presence of marine sedimentary rocks that are composed of calcite and / or dolomite [14-19,21,24,25]. It should be considered that the atmospheric anomalies like the clouds and the mists can also cause relatively high CI as discussed in section 4.1.

The spectral emissivity for silica and silicate rocks (typically igneous rocks) as shown in Figure 3 (b) to (f), demonstrates that the ratio of the emissivity at band 12 or the lower wavelengths to band 13 or the higher wavelengths increases as the chemical SiO_2 content decreases (i.e., as the rock type changes from silicic, felsic to mafic). The ratio value indicates the medium value in the carbonates. To accomplish the separation of the carbonate rocks in the spectral features described above, MI was defined as [13]

$$MI = \frac{D_{12}}{D_{13} \cdot CI^3} = \frac{D_{12} \cdot D_{14}^3}{D_{13}^4}. \tag{4}$$

MI is expected to have an inverse correlation to the chemical SiO_2 content in silicate rocks. It is expected to be high for ultramafic rocks, and to move systematically lower as the rock type changes to felsic, and to be quite low for silicic rocks. Similarly, it has been confirmed high MI is a distinct indicator of ultramafic rocks [14-18,25-30]. Low MI is sensitive for high SiO_2 content rocks with both crystalized and amorphous silica [14,17]. Considering QI is sensitive only for the crystalized quartz, the discrimination between crystalized and disordered quartzose rocks is possible using both QI and MI.

A theoretical analysis on the stability of the indices against the surface temperature and the atmospheric parameters indicated QI and MI are well stabilized against temperature if the atmospheric conditions are good, but CI exhibits a strong dependency to the surface temperature even in atmospherically good conditions [14]. The properties of the indices were confirmed by a practical analysis comparing the results applied to multi-temporal scenes observing a study area [14]. It then showed the effectiveness of normalization processing of the brightness temperature at band 13 to a fixed temperature on improving the heavy dependency of CI to the surface temperature. The normalized radiance registered at the sensor at band i was defined after Planck function as [14,17]

Peer-reviewed version available at Geosciences 2016, 6, 39; doi:10.3390/geosciences6030039

$$nL^{i}_{sen} = L^{i}_{sen} \times \frac{\exp\left\{\frac{\lambda^{13}}{\lambda^{i}} \cdot \ln\left(\frac{c_1}{\pi \cdot \lambda^{13^5} \times L^{13}_{sen}} + 1\right)\right\} - 1}{\exp\left(\frac{c_2}{\lambda^{i} \times nT / \varepsilon_{a^{13}}}\right) - 1}, \quad (5)$$

where the radiation constants $c_1 = 3.742 \times 10^8$ (Wm^{-2}μm^{-4}) and $c_2 = 1.439 \times 10^4$ (μm W), λ^i is the center wavelength (μm) of ASTER band i, (i.e., λ^{10}=8.3, λ^{11}=8.65, λ^{12}=9.1, λ^{13}=10.6, λ^{14}=11.3), L^i_{sen} is radiance registered at the sensor in band i as shown in equation (1), $\varepsilon_a{}^{13}$ is the assumed emissivity in band 13, nT is the fixed temperature (K) to be normalized. In this study, $\varepsilon_a{}^{13}$ is adopted as 1.0, and nT is adopted as 300. This normalization process of the radiance is equivalent to a type of temperature separation processing without atmospheric corrections. That is, as $nL_{sen}{}^{13}$ corresponds to the blackbody radiation of 300K at λ^{13}, when $nL_{sen}{}^{i}$ (equation (5)) is divided with the blackbody radiation of 300K at λ^i, it becomes emissivity with the constant unity value at band 13.

In this paper, the indices QI, CI and MI are calculated on the normalized radiance registered at the sensor data (equation (5)) for the ASTER Level-1B or Level-3A data. One of the reasons using radiance registered at the sensor data (e.g., Level-1B and Level-3A) is the higher availability compared to the emissivity data (e.g., Level-2B04). Another reason is the higher geometrical accuracy in the ortho-rectified image available for the radiance registered at the sensor data (e.g., Level-3A), which is discussed in detail at section 4.2. The Level-2B04 emissivity data are partially applied just for the purpose of the comparison with the Level-1B or Level-3A data within a part of the study area.

2.4. Regional Mapping

The main goal of geological remote sensing requires the mapping of regions containing large-scale structure and lithology and this necessitates the mosaicking of large numbers of satellite scenes. The coverage of one ASTER scene corresponds to approximately 60 km × 60 km on the ground. This is much smaller compared to that of LANDSAT-TM, which has ground coverage approximately 185 km × 170 km. Therefore, the use of ASTER data for geological remote sensing requires the downloading and mosaicking of large numbers of scenes which can become unwieldy. On the other hand, the ASTER data archive is vast and has been actively collecting data for the past 16 years. The procedures to achieve the effective regional lithological mapping with the ASTER mineralogical indices are described below.

Firstly, the browse images of the ASTER data covering the required areas are checked before downloading. In this study, we had obtained ASTER Level-1B products from the JSS site which had closed because of the change in the ASTER data distribution policy which had been announced on April 2016 as described in section 2.2. An alternative method for obtaining ASTER data is to check the browse images and submit an order at the sites of the new distributors (AIST and USGS) [53,54].

The next step is to calculate the indices (i.e., QI, CI and MI) for the respective data, and carefully check the images of the VNIR data and the indices manually. The CI index images should be checked carefully as they can be heavily affected by the atmospheric water content and as a result should be omitted as useless data. During the course of the checking, the priority ranking of each ASTER data is determined, and the mosaic images of the indices covering the area of interest are produced as the regional maps.

In the case of this study, we produce the mosaic images mapped for every 1°×1° region of the Earth surface (hereinafter, we call the region as "tile"), and then joined them together to produce the regional maps covering the entire study area with 54 tiles in total.

More than 10,000 ASTER scenes in archive covering the study area were checked with the browse images, and greater than 5,000 Level-1B images were downloaded. The best 380 Level-1B products were selected to produce the regional maps covering the entire study area.

Peer-reviewed version available at Geosciences 2016, 6, 39; doi:10.3390/geosciences6030039

For the purpose of heightening the value of the geometrical positioning accuracy in the regional maps, each of the Level-1B products constructing the mosaic image is replaced with the Level-3A product of the same ASTER observation. However, the regional maps with the replaced Level-3A products do not cover a part of the area because the coverage of the Level-3A product is a little bit narrower than that of the Level-1B product to ensure the geometrical accuracy. The original Level-1B products are again utilized for the area not covered with the Level-3A products. Finally, the regional maps are consisting of the 380 Level-3A products together with the 6 Level-1B products. In total, the 386 ASTER image products are utilized for composing the regional maps as summarized in appendix Table A1.

3. Results

Figure 4 shows the mosaic color composite image of QI, CI and MI with a linear contrast stretch applied of 0.97-1.055 (QI; Red), 1.005-1.055 (CI; Green), and 0.79-0.95 (MI; Blue) with the ASTER Level-3A products. Two small areas are not covered due to reasons explained in an earlier section. For those areas not covered by the Level-3A products as indicated in Figure 4 with blue polygons, the Level-1B products are alternatively utilized. Annotations have been added using points, lines and rectangles, as shown in Figure 4, indicate the locations which are discussed in the next chapter. Grayscale images with the linear contrast stretches for QI (0.95-1.1), CI (1.005-1.055), and MI (0.75-0.98) were produced using the same ASTER dataset of Figure 4, as shown in Figure 5. The granule ID, observation date and the location at the scene center of the ASTER data products consisting of the regional maps (Figure 4 and 5) are summarized in Table A1, which will be useful in reproducing the results shown here.

To assist readers in locating details of the regional maps, the un-annotated higher-resolution version of the VNIR false color image (Figure 2), the color composite image of the indices (Figure 4), grayscale images of QI (Figure 5 (a)), CI (Figure 5 (b)) and MI (Figure 5 (c)) are presented in the appendix Figures A1 to A5.

Preprints (www.preprints.org) | NOT PEER-REVIEWED | Posted: 9 August 2016 doi:10.20944/preprints201608.0089.v1

Peer-reviewed version available at Geosciences 2016, 6, 39; doi:10.3390/geosciences6030039

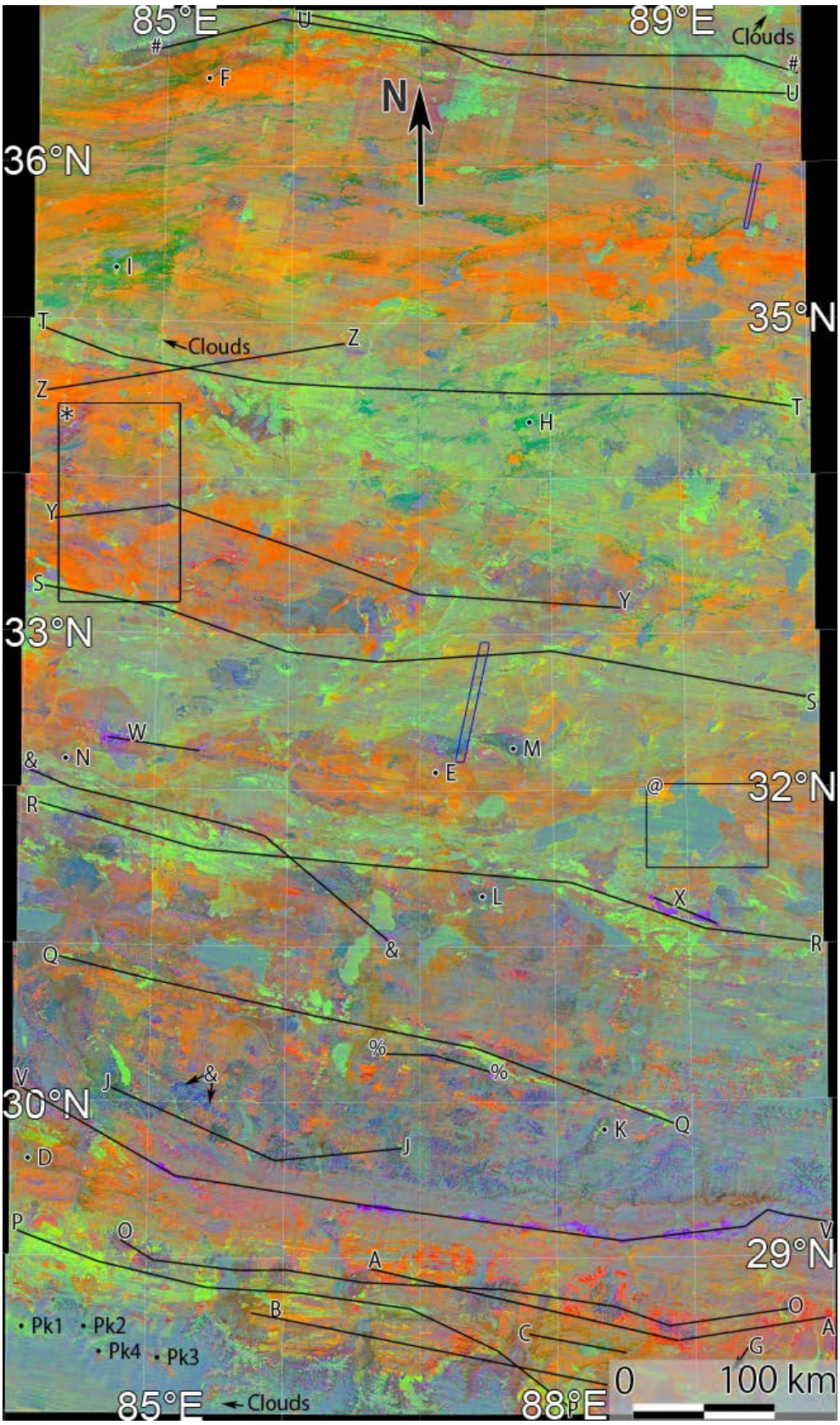

Figure 4. Mosaic color composite image of QI, CI and MI with a linear contrast stretch of 0.97-1.055 (QI; Red), 1.005-1.055 (CI; Green) and 0.79-0.95 (MI; Blue), with ASTER Level-3A products. The areas bounded by the blue polygons are mapped with Level-1B products when Level-3A products were not available. The annotations indicate the locations discussed in the text. The extent of the study area and the map projection are described in the caption in Figure 2.

Preprints (www.preprints.org) | NOT PEER-REVIEWED | Posted: 9 August 2016 doi:10.20944/preprints201608.0089.v1

Peer-reviewed version available at Geosciences 2016, 6, 39; doi:10.3390/geosciences6030039

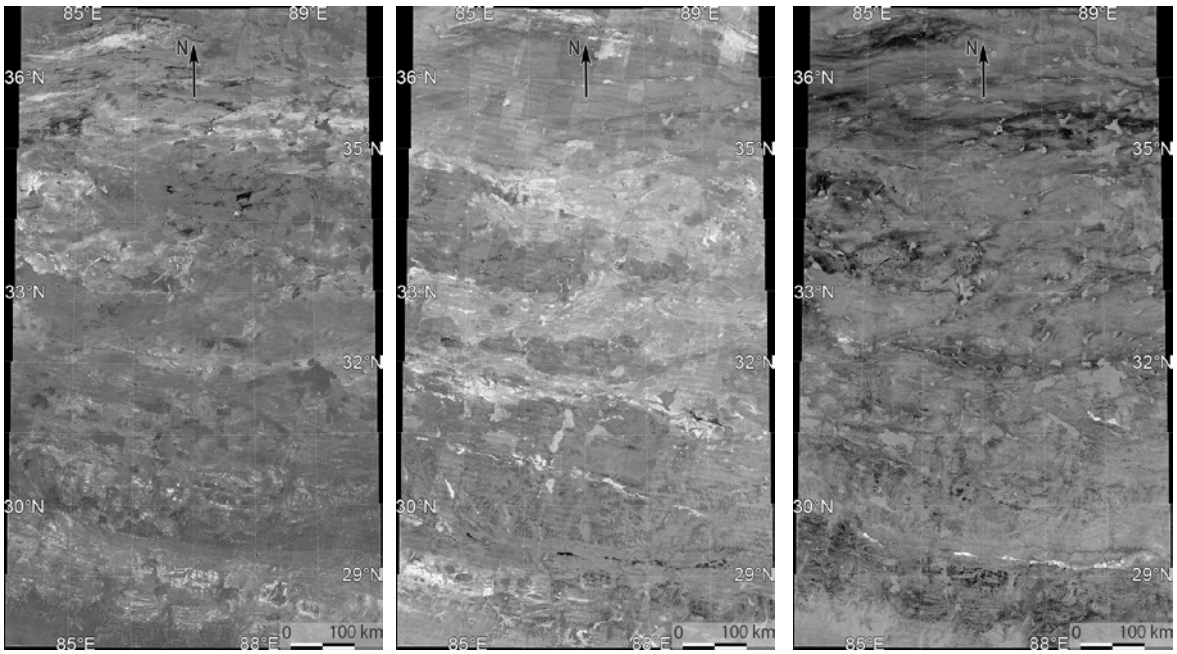

Figure 5. Grayscale image of the indices (a) QI with a linear contrast stretch of the histogram region 0.95 to 1.1, (b) CI with a linear contrast stretch of the histogram region 1.005 to 1.055, and (c) MI with a linear contrast stretch of the histogram region 0.75 to 0.98, produced using the same ASTER dataset of Figure 4 covering the study area. The extent of the study area and the map projection are described in the caption in Figure 2.

4. Discussion

4.1. Properties of Indices for Geological and Other Materials

Many kinds of geological and the other materials are characterized with the indices. To avoid erroneous attention to the colors appeared in the composite image of the indices (Figure 4) for the targets without intensive features in each index (QI, CI or MI; Figure 5), combined use of the grayscale and the color index images (Figures 4 and 5) is essential. Also, to distinguish the geological materials with the other materials (e.g., cloud, vegetation, snow, ice and water) in the images of indices (Figures 4 and 5), it is important to make interpretation referring to the VNIR false color image (Figure 2). In the discussions below, the location of the target is indicated with the annotations in Figure 4. The colors indicated in the discussion are of the composite index image (Figure 4).

High QI (> 1.05) is a distinct indicator of quartz-rich / feldspar-poor rocks, usually quartzose sedimentary rocks [14-17], which are widely distributed in the study area as the whitish pixels in the QI image (Figure 5 (a)). Looking the details, there are several types in the high QI rocks. The high QI rock bodies along the lines "A" show relatively low CI (< 1.02), whereas the most of the others in the northerner part and the ones along the line "B" show intermediate CI (> 1.02) (Figure 5 (a) and (b)). The former look pure reddish and the later do yellowish red (Figure 4). The differences of CI in the high QI rocks can be reflecting the content of carbonates in the quartzose rocks.

Taking notice of the relationship between QI and MI, since MI is designed reversely correlating to the SiO_2 content in the silicate rocks, quartz of 100% SiO_2 content indicates low MI. Specifically, high QI (> 1.05) rocks are simultaneously low MI (< 0.80) (Figure 5 (a) and (c)) in essence, as expected with the spectral property of quartz (Figure 3 (a)). However, high QI (> 1.05) rocks together with intermediate MI (> 0.82) are often observed in and around the distribution area of the high QI / low CI rocks described above, especially along the lines "A". These rocks are expected to be high quartz content coexistent with silicate minerals except feldspars. They are usually

Peer-reviewed version available at Geosciences 2016, 6, 39; doi:10.3390/geosciences6030039

distributed around metamorphic domes in the north Himalayan metamorphic belt [38] discussed later. This type of rocks looks pure to purplish red (Figure 4).

In addition, there are some bodies of intermediate QI (1.02 to 1.04) together with low MI (< 0.80), for example, the ones along the line "C" and around the points "D", "E" and "F" (Figure 5 (a) and (c)). Most of the bodies are in the fluvial deposits as recognized with the VNIR image (Figure 2), and can be non-crystalized-silica-rich deposits in which the spectral features of quartz in ASTER band 10 to band 12 region (Figure 3 (b)) are lost with the weathering processes. These materials look mixed dark reddish (Figure 4). Also, the mixture of quartzose and sulfatic deposits can cause the characteristics of intermediate QI with low MI, which is usual in the northern part of the study area as the sulfate layers are often interbedded within the quartzose layers, as described below.

Low QI (< 0.98) is a distinct indicator for the common sulfate minerals (typically gypsum) [15-17] represented as the blackish pixels in Figure 5 (a). These rocks and deposits, for example, the ones around the points "G", "H" and "I", look deep greenish (Figure 4). We can find the bodies denoting deep greenish color widely in the northern (> 33°N) part of the study area often interbedded within the high QI quartzose layers, which can be the sulfate layers accumulated in the neo-Tethys geological setting. Not as strong as sulfates, but feldspar-rich rocks typically a part of granitic rocks also show low QI [15,17,19]. The bodies around the lines "J" and the point "K" in the Gandise Mountains (annotated in Figure 2), as well as the bodies around the points "L", "M" and "N", are the examples of the rock type with dark bluish green color (Figures 4).

Several types of the intrusive rocks can be discriminated by the combined analysis of the indices with the unique paternal texture information reflecting the geomorphological features of dissection and shape (Figures 4 and 5). One type is the feldspar-rich granitic rock described above. Gabbroic or basaltic rocks are also detectable with the deep bluish color (Figure 4) reflecting the characteristics of relatively high MI (≈0.90) and relatively low QI and CI (Figure 5) [15,17], typically the rock body pointed as "$". Another type is granitic rock related to the north Himalayan metamorphic domes [21,36-38]. The domes are the granitic bodies intruded to the accretion wedges of the south Tibetan detachment system [36], which looks dark pinkish purple color with unique texture and shape (Figure 4) along the line "O". Figure 4 suggests that the metamorphic domes are closely associated with the high QI (>1.05) / low CI (< 1.02) rocks and the high QI (> 1.05) / intermediate MI (0.82 to 0.86) rocks along the lines "A" discussed earlier in this section. According to the previous study [36], the high QI (> 1.05) / low CI (< 1.02) rocks can be linked to low-grade metamorphosed sediments and the high QI (> 1.05) / intermediate MI (0.82 to 0.86) ones to higher-grade ones. More detailed analysis of the indices related to the metamorphic domes with reference to the published articles is presented later at section 4.3.

High CI (> 1.05) is a distinct indicator for the common carbonate minerals, calcite and dolomite [14-17]. The high CI rocks are widely distributed in the study area with the NWW trending, where the ones of around the lines "P", "Q", "R", "S", "T" and "U" are especially prominent (Figure 5 (b)). They look light greenish color (Figure 4). It should be cared the atmospheric water bodies (typically, clouds and mists) also indicate high CI and look light greenish similarly to the carbonate minerals [14-17], as described later.

According to the definition of MI (equation (4)), high MI (> 0.92) is a distinct indicator for the ultramafic rocks with quite low SiO_2 content (< 40 %) [14-17]. High MI bodies are distributed widely in the study area, prominently in the southern part (Figure 5 (c)). They look light purplish color (Figure 4). The ophiolitic ultramafic rocks represent ancient remnants of oceanic lithosphere and underlying upper mantle, which have appeared to the surface suture zones during the course of tectonic activities especially of the subduction of the oceanic plate beneath the continental plate. The most prominent high MI rocks are appeared along the lines "V" (Figures 4 and 5 (c)), which is related to the Indus–Tsangbo Suture (Figure 1). The high MI rocks around the lines "W" and "X" are known related to the Bangong–Nujiang Suture (Figure 1). Not so studied well on the ultramafic exposures related to the other sutures in this study area, i.e., the Longmu Tso–Shuanghu–Menglian–Inthanon, the Jinsha and the East Kunlun suture zones (Figure 1). There are the other high MI bodies, for example, the ones around the lines "Y", "Z" and "#". Additionally,

the ones around the lines "%" and "&" are located in the northern and the southern part of the Lhasa terrane (Figure 1), respectively. The ultramafic rocks also indicate low CI (< 1.02) (Figure 5 (b)), which is another prominent feature in the indices other than high MI (> 0.92). Further analysis on the ultramafic rocks with reference to the published articles is shown later at section 4.3.

Some of the high MI bodies, for example, in and around the rectangle regions "@" and "*", are in the lacustrine deposits. The possible origin is the eroded mafic-ultramafic materials from the ophiolite carried downstream overflowing from the lake [18]. Another possible origin of the high MI signal is the existence of the chloride materials according to the evaporation processes in the deposits, as a part of the chloride materials is known to indicate high MI [17]. Further studies are necessary to be confirmed, however, chlorides could be discriminated with mafic-ultramafic minerals using the feature of relatively high in all the three indices [17].

Considering the characteristics appeared in the indices discussed above, a thematic map is produced by coloring the pixels satisfying given conditions on the indices, as shown in Figure 6. As described above, high QI have been confirmed to be a distinct indicator for high-quartz / low-feldspar sedimentary rocks [14-19,21-23,26,29,30], but this study presents the first attempt to classify within the high QI rock bodies. The high QI (> 1.05) bodies are divided into three classes with the conditions on CI and MI. The first class is for low MI (< 0.80) / medium CI (> 1.02), the second class is for low MI (< 0.80) / low CI (<1.02) and the third class is for relatively high MI (> 0.82). Further discussion on the discriminations in the high QI bodies related to the metamorphic domes is made at section 4.3.

Figure 6 shows the thematic mapping for 8 classes of possible rock types, i.e., high-quartz / low-silicates with some carbonates, high-quartz / low-silicates with minor carbonates, high-quartz / low-feldspars with some mafic minerals, carbonates, sulfates, sulfate- or feldspar-rich, ultramafic and mafic-ultramafic. This map suggests well detection of each rock type with the given criteria on the indices.

The criterion to detect ultramafic rocks adopted in Figure 6 is MI > 0.92, which have been confirmed as the distinct one [14-17]. Since there are not so many high MI bodies in the northern half of the study area, relatively low criterion, MI > 0.905, is adopted for the mafic-ultramafic rocks to detect more candidates of the targets. That is why many pixels are erroneously detected as colored blue in Figure 6, especially in the southern part of the study area.

For the purpose of assisting readers in locating details of the figure, the higher resolution version of Figure 6 without the legends and annotations is given in the appendix Figure A6.

Preprints (www.preprints.org) | NOT PEER-REVIEWED | Posted: 9 August 2016 doi:10.20944/preprints201608.0089.v1

Peer-reviewed version available at Geosciences 2016, 6, 39; doi:10.3390/geosciences6030039

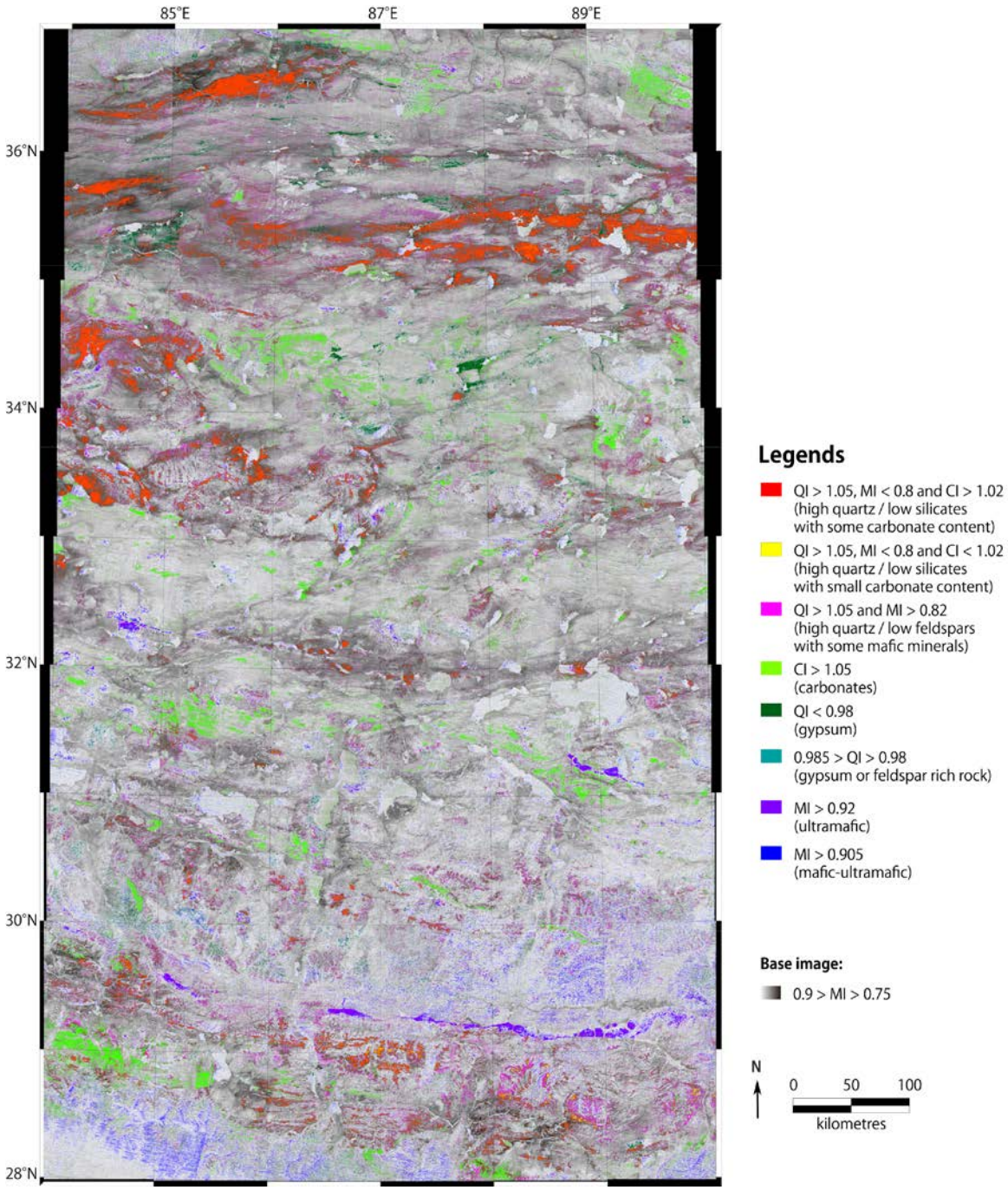

Figure 6. Detected possible rock types colored for each pixel with the given conditions (see legend) on the indices mapped on the grayscale image of MI (0.75-0.9)

As shown in the VNIR false color image (Figure 2), a lot of lakes are distributed in this study area. The CI image (Figure 5 (b)) indicates the surface water bodies of the lakes take various values in CI, which perhaps reflects the status (solid or liquid), the temperature, and the composition of the water and so on. Further studies are necessary for clarifying the reason of taking wide range in CI for the surface water bodies.

The CI is very sensitive to the atmospheric water as described in section 2.4. The bodies with high concentration of the atmospheric water indicate high CI, similarly to the carbonate minerals. We can detect the clouds with the VNIR image (Figure 2). However, the bodies concentrated with water vapor are not detectable with VNIR. Therefore, it is important to compare the multi-temporal images of CI. If the features are stably appearing through the multi-temporal images, they are reflecting the surface materials. Elsewise, the features are caused by the atmospheric water

Peer-reviewed version available at Geosciences 2016, 6, 39; doi:10.3390/geosciences6030039

concentrations. In this study, we tried to find cloud-free ASTER data as much as possible. However, there are still several small fractions of clouds in the maps, for example, around the points (28.1°N, 85.5°E), (34.9°N, 85.0°E) and (37.0°N, 89.75°E), annotated as "Clouds" in Figure 4. The clouds, as well as a part of snow, ice and lakes, are detected as high CI pixels in Figure 6.

There are many snow or ice bodies do not disappear all through the years as shown in the VNIR image (Figure 2), although other snow bodies are usually easy to be disappeared because of the high evaporating rate at the study area located in the world highest altitude region. These deep snow or ice bodies usually look whitish green (Figure 4) with relatively high CI. Many glacier bodies are observed in this study area, especially in the Himalaya Mountains, as shown in the VNIR image (Figure 2). It is not possible to get any features in the optical remote sensing data for the materials completely covered with. However, we can retrieve the meaningful signals around the bodies. For example, the lithological features around the peaks of the Annapurna II, the Manaslu, the Ganesh I and the Ngadi Chuli in the Himalaya Mountains (annotated as "Pk1", "Pk2", "Pk3" and "Pk4" in Figure 4, respectively) can be drawn from the maps of the indices (Figures 4 and 5). Despite the area around the peaks is covered with snow or ice as observed in the VNIR image (Figure 2), the indices suggest the major layers around the Mt. Annapurna II are carbonate (light greenish bodies) with the minor layers of quartz (reddish bodies). On the other hand, Figure 4 suggests many kinds of layers distributed around the Manaslu Mountains. The peak region appears to be carbonate rocks (light greenish bodies), and the regions around the glacier valleys in the south western part of the peak to be feldspar-rich granitic rocks (dark greenish bodies). The lithological features in the indices around the Ngadi Chuli peak ("Pk4") located south of the Mt. Manaslu are similar to the ones around the Ganesh I peak ("Pk3"). It suggests the alternation of quartzose and carbonate layers expected in the areas. Further studies are necessary for solider lithological interpretation with the indices in the Himalaya Mountains region.

The VNIR image (Figure 2) indicates that the south-western part of the study area in the southern slopes of the Himalaya Mountains in Nepal is heavily covered with vegetation. Most of the signals in the indices are obscured by vegetation, however, we can find some signals in the indices (Figures 4 and 5) along the valleys of the rivers in the area, which are possibly geologically meaningful.

The characteristics of the indices for the geological and the other materials in the study area discussed above are summarized in Table 1.

Table 1. Characteristics of the indices for geological and the other materials

Expected material	Typical geology in the study area	Features in indices (Fig 5)	Color in index image (Fig 4)	Detectability with VNIR (Fig 2)	Generality
Quartz rich / Feldspars poor	Quartzose sedimentary rocks	QI>1.05	Pure to yellowish red	Not clear	Confirmed [14-19, 21-23, 26, 29, 30]
Quartz rich / Silicates poor with some carbonates	Quartzose sedimentary layers related to Tethys	QI>1.05, MI<0.8 and CI>1.02	Yellowish red	Not clear	Not yet (this study is the first attempt)
Quartz rich / Silicates poor with minor carbonates	Low-grade metamorphic sediments around intrusions	QI>1.05, M<0.8 and CI<1.02	Pure red	Not clear	Not yet (this study is the first attempt)
Quartz rich / Feldspars poor with some mafic minerals	Higher-grade metamorphic sediments around intrusions	QI > 1.05 and MI > 0.82	Red to purplish red	Not clear	Not yet (this study is the first attempt)

Peer-reviewed version available at Geosciences 2016, 6, 39; doi:10.3390/geosciences6030039

Carbonates	Marine sedimentary layers related to Tethys	CI > 1.05	light green	Not clear	Confirmed [14-19, 21, 24, 25]
Sulfates	Evaporates related to neo-Tethys	QI < 0.98	Deep green	Not clear	Confirmed [15-17, 30]
Ultramafic	Ophiolites related to sutures	MI > 0.92	Light purple	Not clear	Confirmed [14-18, 25-30]
Feldspars rich granitic rocks	Granitic rocks related to island arc (e.g., Gandise batholith)	Relatively low QI / Image pattern	Dark bluish green	Not clear	Partially confirmed [15, 17, 19, 30]
Feldspars poor granitic rocks	Granitic rocks related to metamorphic domes	Image pattern	Dark pinkish purple	Not clear	Not yet (this study partially attempts)
Mafic rocks	Basalt and gabbro	Relatively high MI (≈0.90)	Deep blue	Not clear	Partially confirmed [15, 17]
Atmospheric water	-	High CI	Light green	Partially (for clouds)	-
Snow and ice	-	Relatively high for all the indices	Whitish green	Yes	-
Vegetation	-	Relatively high MI (≈0.89)	Greenish blue	Yes	-
Lake water	-	Relatively high MI (≈0.89), Various values in CI	Various blue to light green colors	Yes	-

4.2 Geometrical and Radiometric Performance

Since the ASTER observes with the pointing angle up to ±8.55° (for SWIR and TIR subsystems; ±24° for the VNIR subsystem) in the plane vertical to the moving direction of the satellite [44], the geometrical error caused by the parallax effect in the Level-1B and the series of Level-2B data can be one sixth of the elevation at the target. As the study area covers the world highest region of the Tibetan Plateau and the Himalaya Mountains, the parallax effect is quite significant. On the other hand, the ortho-rectified Level-3A data are corrected for the geometrical errors. Comparing the images covering a part of the study area at just the north of the Everest peak (Figure 7), the positional mis-registration in the Level-1B and the Level-2B04 images is indicated as shown below. For the sub-area "A" indicated in Figure 7, the single rock unit shown in the Level-3A image (pointed with an arrow in Figure 7 (c)) is observed double (pointed with two arrows in Figure 7 (a) and (b), respectively). Likewise for the sub-area "B", the lithological boundary between the dark bluish green unit and the dark pinkish purple unit shown across the yellow line in Figure 7 (c) is overlapped and missed a part of the area in (a) and (b) as indicated with the yellow arrows on the line. These suggest the mis-registration by the parallax effect occurred for Level-1B and Level-2B products, which are corrected for Level-3A product.

Peer-reviewed version available at Geosciences 2016, 6, 39; doi:10.3390/geosciences6030039

The mosaic index image of Level-1B data (Figure 7 (a)) and the one of Level-2B04 (Figure 7 (b)) are almost identical into details, which suggests the radiometric performance of the mosaic index map with the radiance registered at the sensor data (i.e., Level-1B or Level-3A) is not inferior to the one with emissivity (i.e., Level-2B04). The boundary of the scenes composing the mosaic map is not significant in any cases of Figure 7 (a) and (b).

Considering the geometrical and radiometric performances on the ASTER data and the indices discussed above, using the ortho-rectified radiance registered at the sensor data (e.g., Level-3A) is obviously advantageous in the mosaic lithological mapping of this study.

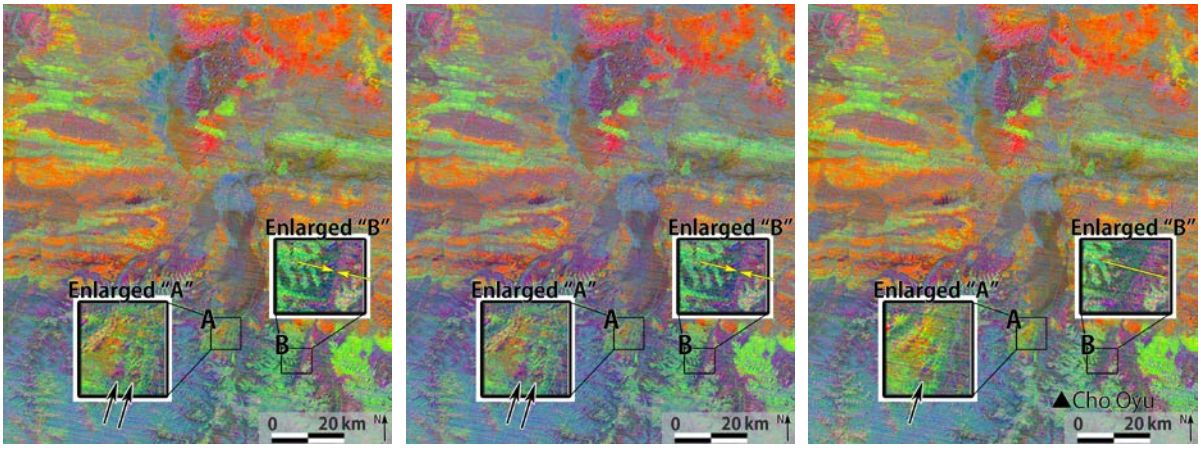

(a) (b) (c)

Figure 7. Mosaic color composite image of QI, CI and MI covering the region bounded by the latitude 28° to 29° North and the longitude 86° to 87° East with (a) ASTER Level-1B products, (b) ASTER Level-2B04 products and (c) ASTER LEVEL-3A products. The coverage in the study area is indicated as yellow rectangle in Figure 2. A linear contrast stretching of 0.97-1.055 (QI; Red), 1.005-1.055 (CI; Green) and 0.79-0.95 (MI; Blue) is applied on (a) and (c), and 0.975-1.085 (QI; Red), 1.09-1.145 (CI; Green) and 0.76-0.96 (MI; Blue) is applied on (b). The sub-areas "A" and "B" are enlarged for pointing out the parallax effects. For "A", the rock unit shown in (c) indicated with an arrow is observed double in (a) and (b) as indicated with two arrows. For "B", the lithological boundary shown across the yellow line in (c) is overlapped and missed a part of area along the boundary in (a) and (b) as indicated with the yellow arrows on the line. These suggest the geometrical mis-registration by the parallax effect occurred for Level-1B and Level-2B products, which are corrected for Level-3A product. The location of Mt. Cho Oyu is indicated in (c).

4.3. Geological Interpretation on the Results

The characteristics found in the indices (i.e., QI, CI and MI) are discussed in detail at section 4.1, and summarized in Table 1. Also, a thematic map related to the target rock types is produced with the basis on the discussion, as shown in Figure 6. In this section, we show more detailed mapping for the high MI mafic-ultramafic rock bodies and the high MI lacustrine deposits within the entire study area, and the metamorphic domes [21,36,37] located in the north Himalayan metamorphic belt [38]. These detailed analyses are made by considering the result maps (i.e., Figures 2, 4, 5 and 6) and the discussion at section 4.1 totally, as shown in Figure 8. A part of these mapping results of the target rocks is compared with the field investigations published so far.

Preprints (www.preprints.org) | NOT PEER-REVIEWED | Posted: 9 August 2016 doi:10.20944/preprints201608.0089.v1

Peer-reviewed version available at Geosciences 2016, 6, 39; doi:10.3390/geosciences6030039

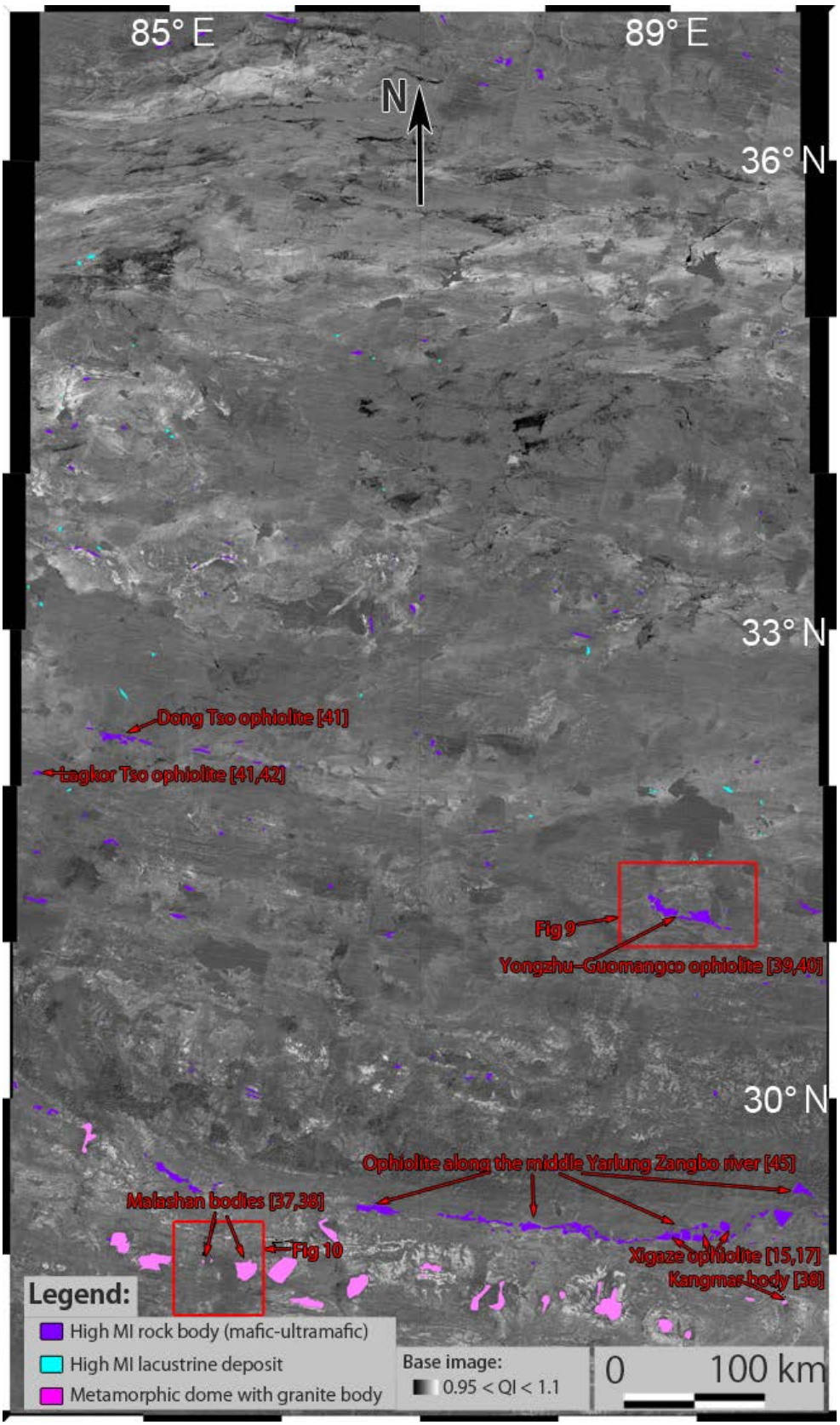

Figure 8. Distribution map for high MI mafic-ultramafic rock bodies, high MI lacustrine deposits and metamorphic domes cored with granite, interpreted with the mosaic images of the indices (Figures 4 and 5), VNIR (Figure 2) and the thematic map with the indices (Figure 6) superimposed on the grayscale image of QI. The red rectangle represents the coverage of Figures 9 and 10. The information of the previous articles with local geological investigations is embedded as the red arrowed lines and texts.

Peer-reviewed version available at Geosciences 2016, 6, 39; doi:10.3390/geosciences6030039

The clearly detectable high MI ultramafic rocks related to the Indus–Tsangbo Suture (ITS; along the lines "V" in Figure 4), and the ones of the Yongzhu–Guomangco section and the Dong Tso section related to the Bangong–Nujiang Suture (BNS; along the lines "W" and "X", respectively, in Figure 4) are mapped according to the criterion of MI > 0.92 accomplished in Figure 6. The other high MI bodies are recognized with the criterion MI > 0.905. Considering the spatial extent of the detected bodies checking with the result maps, especially Figures 4 and 5 (c), it is determined whether target or not. Considering with the VNIR image (Figure 2), the detected high MI bodies are discriminated between mafic-ultramafic rocks and lacustrine deposits, as shown in Figure 8.

The distribution map of the ultramafic rocks given in this study using the ASTER-TIR data (Figure 8) agrees well with the published maps [39-41,44]. Ninomiya et al. [15,17] suggested the high correlation of the detected ultramafic rocks using ASTER-TIR data with the ones described in the published ophiolite map along the middle Yarlung Zangbo river [44] for the local area south of Xigaze (indicated in Figure 8), but this study suggests the agreement within the entire region of the map. Likewise, the good agreement in the mapping results for the ultramafic rocks of Yongzhu–Guomangco section [39,40], Dong Tso section [41] and Lagkor Tso section [41,42] is suggested.

The strong point of mapping with remote sensing over the one with field survey is the heterogenetic observability at the constant interval regardless the accessibility. On the other hand, whereas the field survey is limited to the area along the accessible routes, it observes many kind of matters, for example, slant and dip of the stratigraphy to reconstruct geology in three dimensions, fossils and radioactive isotope contents in the hand samples to determine age and so on, which are not possible to measure with remote sensing. In that sense, the lithological mapping with remote sensing complements the field geological survey for the materials detectable with the remote sensors in the condition where the rocks are appeared at the surface over vegetation, snow, and glacier and so on. Concerning this case study with ASTER-TIR, it can support improving geological mapping of the materials listed in Table 1, especially of quartz-rich / feldspar-poor rocks, carbonate rocks, ultramafic rocks and sulphatic rocks, which are confirmed to be detected distinctly with the indices as described in section 4.1 and Table 1.

Figure 9 shows the comparison of the mapped ultramafic-mafic rocks by this study (Fig. 9 (a)) with the published geological map in scale of 1:250,000 [40] (Fig. 9 (b)). The ASTER image shows that the ultramafic-mafic rocks distribute along the NW-striking fault zones and provides a more detailed spatial distribution comparing with the conventional geological mapping. Additionally, after the specific features for the granitic rocks discussed in section 4.1 and summarized in Table 1, the granitic intrusive bodies in the east of Guomangco Lake are mapped in Figure 9 (a), which denote dark greenish blue color with unique texture and shape in the color index image (Figure 4). The color index image (background image of Figure 9 (a) cut and enlarged from Figure 4) also indicates the distribution of quartzose and carbonate sediments, which denote yellowish red and light green, respectively. These mapping results suggest that ASTER-TIR index images (Figures 4 and 5) can provide an efficient approach to make mapping of the rock types in remote and inaccessible Tibetan Plateau with an average elevation of over 4,500 meters.

Peer-reviewed version available at Geosciences 2016, 6, 39; doi:10.3390/geosciences6030039

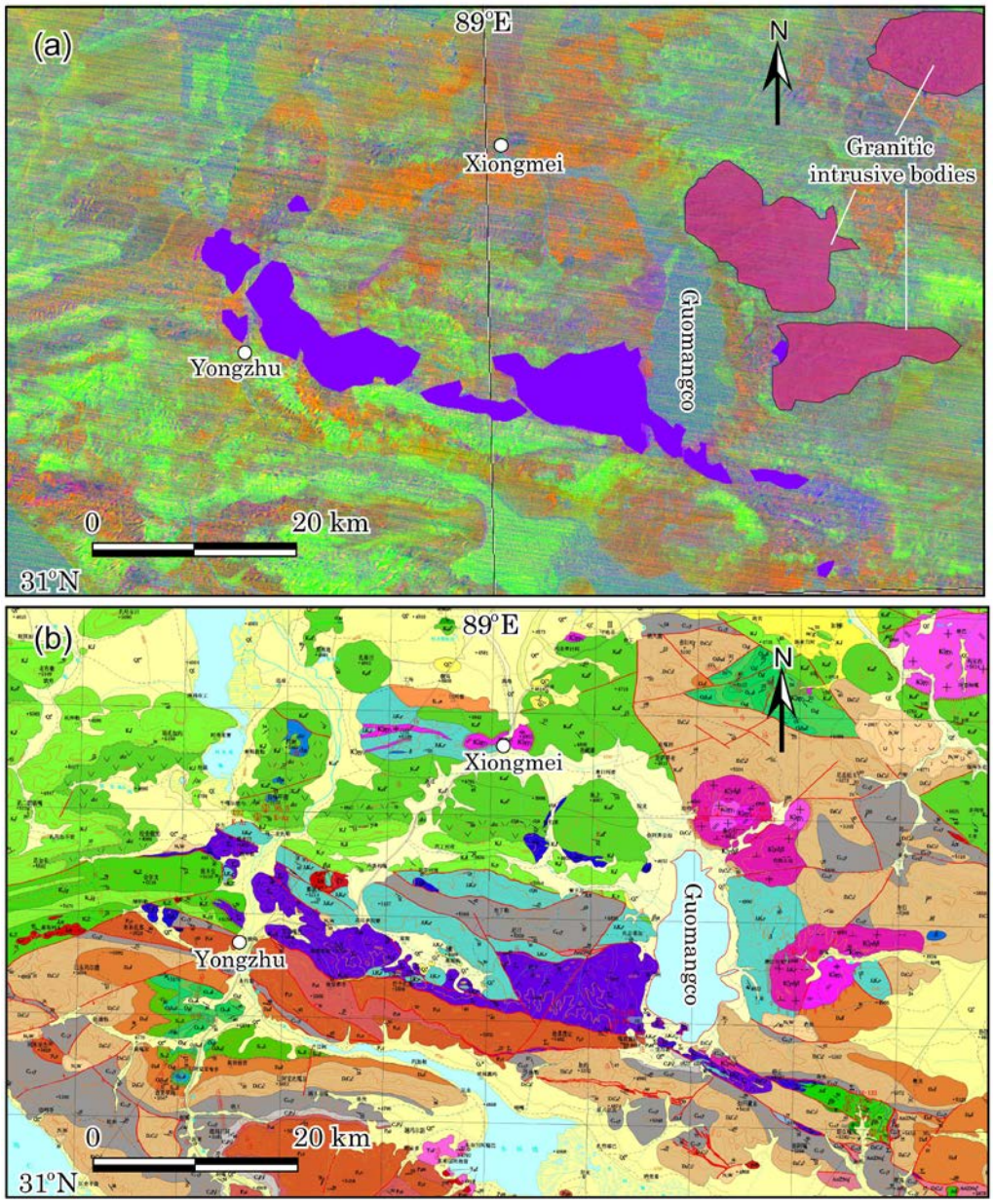

Figure 9. Comparison of (a) the Yongzhu–Guomangco ophiolite map (the polygons colored purple; enlarged from Figure 8) and the map of the granitic intrusive bodies (the polygons colored reddish purple) derived in this study using ASTER TIR data superimposed on the color composite image of the indices (Figure 4) with (b) the published geological map based on the field investigations (e.g., [39,40]). The coverage of this figure is shown as the red rectangle in Figure 8.

Figure 8 also maps the rock bodies related to the north Himalayan metamorphic domes [21,36-38] intruded during Cenozoic to the accretion wedges of the south Tibetan detachment system, located in the E-W direction in the Himalaya terrane at the southern part of the Indus–Tsangbo Suture. According to the compiled map by Burrell et al. [36] with the published 1:1,500,000 scale geological map [44], granite and granitic gneiss at the core of the domes are accompanied with high-grade metamorphosed gneissose sediments around the core and low-grade metamorphosed sediments around the gneiss in the eastern half region (in longitude 87° E and easterner). On the other hand, it is not so well accompanied with those high-grade and low-grade metamorphosed rocks in the western half region (in longitude 87° E and westerner).

As discussed in section 4.1, the characteristics of the indices for the kind of granitic rocks are not so distinct at the individual pixels, however, it can be mapped considering together with the unique shape and paternal textures recognized in the images of the indices (Figures 4 and 5). As

Peer-reviewed version available at Geosciences 2016, 6, 39; doi:10.3390/geosciences6030039

summarized in Table 1, granitic rocks with relatively high feldspar content look dark bluish green color in the index image (Figure 4). On the other hand, the dominant granitic rocks distributed related to the domes look dark pinkish purple (Figure 4). This color is probably reflecting lesser feldspar content. The relatively feldspar-rich granitic rocks of dark bluish green color (Figure 4) are also widely distributing in this region related to the domes.

Comparing the colors of the targets (i.e., the rocks associated with the domes) in the image of the indices (Figure 4) with the previous studies [21,36-38] and the geological map [44], we assume that the dark pinkish purple bodies correspond to the cored and the high-grade metamorphosed granitic rocks. Likewise, we assume the correspondences of the dark bluish green bodies to the feldspar-rich granitic rocks, the pinkish red bodies to the high-grade metamorphosed sediments and the pure reddish bodies to the low-grade metamorphosed sediments, respectively. The mapped granitic bodies in Figure 8 are just only for the ones with dark pinkish purple color, because they are the most prominent target characterizing the metamorphic domes. The similar kind of the bodies in the Himalaya Mountains and the Gandise Mountains are omitted from the mapping (Figure 8). However, the body at the southern part of Mt. Loinbo Kangri (indicated in Figure 2), which is not mapped previously [36-38,45] for recognized as a part of Gandise granitic rock group, is included to this map (Figure 8) because it is located at just south of the Gandise Mountains within the Tethyan quartzose and carbonate sediments related to the south Tibetan detachment system as suggested in Figure 4. As this study is the first case to attempt detecting these kinds of the rock types with the indices, the generality of which is not confirmed so far yet (Table 1), the mapping result of the metamorphic domes shown in Figure 8 presents a preliminary case.

The Kangmar dome and the western portion of the Malashan dome, the locations of which are indicated in Figure 8, are the best investigated ones with the previous studies [37,38]. They are dominated with the dark bluish green (Figure 4) bodies assumed here as the feldspar-rich granitic rocks. On the other hand, the most of the other domes are dominated with the dark pinkish purple bodies which are assumed here as the relatively feldspar-poor granites and its high-grade metamorphosed ones. As the target of mapping in this study (Figure 8) is the latter, very small bodies are mapped for the Kangmar and the western Malashan units compared to the published maps [36,45].

Several domes are newly mapped in Figure 8 additionally to the known ones mapped so far [36,45], typically the one just west of Kangmar dome (Figure 8). Further augments are necessary in field for the validity of the new mapping.

According to the Figures 4 and 6, most of the domes are accompanied with the Tethyan quartzose sediments of the pinkish red bodies (Figure 4) assumed here as high-grade metamorphosed sediments and reddish bodies (Figure 4) assumed here as low-grade metamorphosed sediments. Figure 4 suggests that the association is more obvious for the domes in the eastern half of the region comparing to the ones in the western half, as indicated by Burrell et al. [36]. Probably, the reason of the difference is because the domes in the eastern half region are intruded to the accretion wedges dominated with quartzose sediments, on the other hand, the ones in the western half are intruded to the ones dominated with carbonate sediments as inferred from the index map (Figure 4).

Figure 10 shows the comparison of the lithological mapping using the color index image (Figure 4) with the geological summary map investigated by Aoya et al. [37] around the western Malashan dome located in the western shore region of Paiku Lake. This figure indicates good agreement between our result and Aoya's one. The spatial extents for some of the geological bodies are more detailedly mapped in this study as expected with the strong points of remote sensing described earlier in this section. On the other hand, it is difficult to distinguish between two-mica granites and leucogranites with the approach of this study, which is inferred as the difference of the chemical or mineral composition in the two types of granite is not as significant as detectable with ASTER-TIR. Some high QI bodies detected as quartzose sediments in the map of this study (Figure 10 (a)), for example the one just west of the Paiku leucogranite body, is classified as calc schist in Aoya's map (Figure 10 (b)). The units mapped as pelitic schist in Aoya's map correspond well to the

Preprints (www.preprints.org) | NOT PEER-REVIEWED | Posted: 9 August 2016 doi:10.20944/preprints201608.0089.v1

Peer-reviewed version available at Geosciences 2016, 6, 39; doi:10.3390/geosciences6030039

high QI /relatively low CI bodies with pure reddish color in the map of this study (Figure 10 (a)) assumed here as low-grade metamorphosed quartzose sediments.

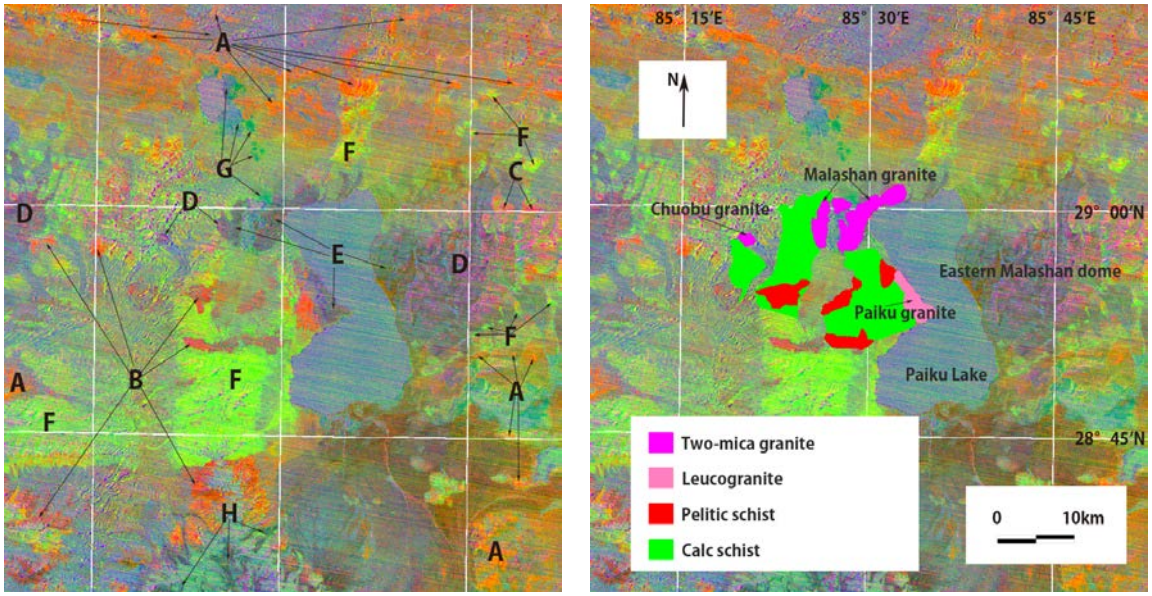

(**a**) (**b**)

Figure 10. (a) Lithological mapping with the mosaic color composite image of QI, CI and MI around the Malashan domes. The coverage of this image is indicated in Figure 8. The interpreted rock types with this image are A: Quartzose sedimentary layers related to the Tethys, colored yellowish red; B: Low-grade metamorphic quartzose Tethyan sediments related to the intrusion, colored pure red; C: High-grade metamorphic quartzose Tethyan sediments around metamorphic domes, colored pinkish red; D: Relatively feldspars poor granitic rocks related to the domes, colored dark pinkish purple; E: Feldspars rich granitic rocks around the domes, colored dark bluish green; F: Carbonate layers related to the Tethys, colored light green; G: Sulfate deposits, colored deep green; H: Feldspars rich granitic rocks at the glacier valleys in the north slope of Himalaya Mountains. (b) Geological map around the western Malashan metamorphic dome area investigated by Aoya et al. [37] embedded in the color composite image of the indices.

Apart from the geological units mapped by Aoya et al. [37], there are many lithological features mappable with the color index image (Figure 10 (a)) where alphabetic symbols are annotated in the figure to indicate the targets. As described in section 4.1 and summarized in Table 1, quartz-rich / feldspar-poor layers, carbonate layers and sulfate deposits are distinctively detected as "A" to "C", "F" and "G", respectively, according to the colors based on the features in the indices. Feldspar-rich granitic rocks detected at "E" and "H" are discriminated with another type of granitic rocks detected around "D" which are mapped as metamorphic dome in Figure 8, as the color for the former is dark bluish green whereas for the latter is dark pinkish purple. This is the first study of the latter granitic rocks with reference to the indices for ASTER-TIR data. Also, this study attempts classifying the high QI layers into three classes, i.e., relatively high CI / low MI layers assumed here as non-metamorphosed quartzose sediments, relatively low CI / low MI layers assumed here as low-grade metamorphic quartzose sediments, and relatively high MI layers assumed here as high-grade metamorphic quartzose sediments. In Figure 10 (a), these rock types are distributed at "A", "B" and "C", respectively. The materials detected with the features in the indices given in this study for the first time are determined under assumptions, which should be confirmed with the field investigations.

As a summary, although much of the information inevitable for geological mapping is acquired only with the field investigations, complemental use of this approach will improve the quality of mapping in detecting the exact spatial extent of the target materials of this study.

5. Conclusions

ASTER TIR mineralogical indices, i.e., QI, CI, and MI, were defined on the basis of the spectral properties of typical geological materials and applied to a large central region of the Tibetan Plateau. The advantages of using the ortho-rectified radiance registered at the sensor data (e.g., Level-3A products) were discussed in addition to sensor geometrical and radiometric performances. The maps were interpreted to accomplish more detailed mapping of ultramafic rock bodies and north Himalayan metamorphic granite bodies. This study sought to differentiate granitic rock types according to the abundance of feldspars, as well as the classification of the quartzose sedimentary layers according to the content of carbonates and mafic minerals. Results indicate that lithological mapping using TIR spectral indices were successful in detecting quartzose sedimentary, carbonate, and sulphatic layers, in addition to ultramafic bodies, which had been confirmed from previous remote sensing investigations. The results from the detailed mapping were compared to prior field-based geological mapping studies and it was found that they also agreed well. The advantage of using remote sensing to detect the spatial extent of the target materials, i.e., its superiority over conventional geological mapping, has been well established. However, the geological materials detected using these described techniques need to be confirmed through a vigorous campaign of ground-based field investigations. A further survey is planned where the regional lithological mapping will be applied to the entire Tibetan Plateau, as well as to areas in northwestern China, such as the Tarim Basin and the surrounding area.

Acknowledgments: The ASTER data used in this study are supplied by Japan Space Systems. ASTER data are credited to NASA/METI/AIST/Japan Space Systems, and U.S./Japan ASTER Science Team. Comments of Robert Corrie, The Queen's College, University of Oxford and Koki Iwao, AIST, as well as of the four anonymous reviewers and the academic editors, have substantially improved the manuscript. This work was supported by the Strategic Priority Research Program of the Chinese Academy of Sciences (Grant No. XDB03020200).

Author Contributions: Y.N. performed the ASTER data processing. B.F. prepared the description of the geological setting of the study area. Y.N. and B.F. collaboratively discussed on the results. B.F. prepared Figures 1, B.F. and Y.N. cooperatively prepared Figure 9, and Y.N. prepared the other figures.

Conflicts of Interest: The authors declare no conflict of interest.

Abbreviations

The following abbreviations are used in this manuscript:

ASTER: Advanced Spaceborne Thermal Emission and Reflection Radiometer
VNIR: Visible and Near Infrared
TIR: Thermal Infrared
QI: Quartz Index
CI: Carbonate Index
MI: Mafic Index
JSS: Japan Space Systems

Peer-reviewed version available at Geosciences 2016, 6, 39; doi:10.3390/geosciences6030039

Appendix

Table A1. The list of the ASTER products composing the produced regional maps (Figure 4 and 5).

1°×1°tile's South-western corner [(latitude, longitude)]	JSS Granule ID[1,2] of ASTER product used for mapping, listed in the order of priority	Observation date [yyyymmdd]	Latitude at the scene center [°N]	Longitude at the scene center [°E]	Number of products (number redundant) for Level-3A, Level-1B
(37°N, 84°E)	AST3A1 030903050857120615 0053	20030903	35.90	84.91	10(0), 0(0)
	AST3A1 011116051330120615 0006	20011116	36.98	85.07	
	AST3A1 011116051339120615 0010	20011116	36.45	84.92	
	AST3A1 011116051347120615 0055	20011116	35.91	84.78	
	AST3A1 071115052131120615 0007	20071115	36.09	84.26	
	AST3A1 061121051458120615 0011	20061121	36.80	84.75	
	AST3A1 071115052122120615 0012	20071115	36.62	84.42	
	AST3A1 080306052129120615 0015	20080306	37.21	84.19	
	AST3A1 080306052138120615 0017	20080306	36.68	84.03	
	AST3A1 080203052158120615 0021	20080203	36.10	84.20	
(37°N, 85°E)	AST3A1 031028051539120615 0051	20031028	36.16	85.38	12(1), 0(0)
	AST3A1 060918051455150717 0001	20060918	37.15	86.11	
	AST3A1 010702052324150717 0001	20010702	37.22	85.68	
	AST3A1 030903050848120615 0009	20030903	36.42	85.05	
	*AST3A1 030903050857120615 0053	20030903	35.90	84.91	
	AST3A1 031028051530150717 0001	20031028	36.69	85.54	
	AST3A1 030903050839150717 0001	20030903	36.96	85.20	
	AST3A1 030802050837150717 0001	20030802	36.26	86.21	
	AST3A1 030802050846150717 0001	20030802	35.73	86.05	
	AST3A1 001129052222150717 0001	20001129	36.28	86.13	
	AST3A1 020923051658150717 0001	20020923	36.64	85.84	
	AST3A1 001104052900150313 0001	20001104	36.10	85.74	
(37°N, 86°E)	AST3A1 010711051717150717 0001	20010711	37.23	87.14	9(3), 0(0)
	AST3A1 010711051726150717 0001	20010711	36.70	86.98	
	AST3A1 010711051735150714 0001	20010711	36.17	86.82	
	AST3A1 020916051051150717 0001	20020916	36.76	86.59	
	*AST3A1 060918051455150717 0001	20060918	37.15	86.11	
	AST3A1 030802050828150717 0001	20030802	36.79	86.36	
	*AST3A1 030802050837150717 0001	20030802	36.26	86.21	
	*AST3A1 030802050846150717 0001	20030802	35.73	86.05	
	AST3A1 001129052213150717 0001	20001129	36.81	86.28	
(37°N, 87°E)	*AST3A1 010711051735150714 0001	20010711	36.17	86.82	13(3), 0(0)
	*AST3A1 010711051726150717 0001	20010711	36.70	86.98	
	*AST3A1 010711051717150717 0001	20010711	37.23	87.14	
	AST3A1 030719045614150716 0001	20030719	36.96	88.26	
	AST3A1 030719045623150716 0001	20030719	36.43	88.11	
	AST3A1 030719045631150714 0001	20030719	35.90	87.97	
	AST3A1 011024050826150717 0001	20011024	36.82	87.70	
	AST3A1 011024050843150714 0001	20011024	35.76	87.39	
	AST3A1 001028052244150717 0001	20001028	37.16	87.59	
	AST3A1 001028052253150717 0001	20001028	36.63	87.42	
	AST3A1 001028052302150714 0001	20001028	36.11	87.26	
	AST3A1 051028045616150716 0001	20051028	36.45	87.97	
	AST3A1 051028045625150714 0001	20051028	35.92	87.82	
(37°N, 88°E)	AST3A1 020411045810150716 0001	20020411	36.86	89.03	9(3), 0(0)
	AST3A1 020411045819150716 0001	20020411	36.33	88.88	

Peer-reviewed version available at Geosciences 2016, 6, 39; doi:10.3390/geosciences6030039

	AST3A1 020411045828150714000l	20020411	35.80	88.73	
	AST3A1 040331045716150714000l	20040331	35.85	88.34	
	*AST3A1 030719045614150716000l	20030719	36.96	88.26	
	*AST3A1 030719045623150716000l	20030719	36.43	88.11	
	*AST3A1 030719045631150714000l	20030719	35.90	87.97	
	AST3A1 070916045713150716000l	20070916	36.93	88.49	
	AST3A1 070916045722150716000l	20070916	36.40	88.34	
(37°N, 89°E)	AST3A1 000912051213150716000l	20000912	35.78	88.85	9(0), 0(0)
	AST3A1 000912051204150716000l	20000912	36.31	89.00	
	AST3A1 000912051155150716000l	20000912	36.84	89.16	
	AST3A1 061008045006150716000l	20061008	36.91	90.21	
	AST3A1 030921045633150716000l	20030921	36.68	90.22	
	AST3A1 030921045642150714000l	20030921	36.15	90.06	
	AST3A1 011010045649150714000l	20011010	35.93	89.32	
	AST3A1 071221045701150716000l	20071221	36.75	89.76	
	AST3A1 071221045710150716000l	20071221	36.22	89.60	
(36°N, 84°E)	*AST3A1 030903050857120615005 3l	20030903	35.90	84.91	12(3), 0(0)
	AST3A1 030903050906120615005 6l	20030903	35.37	84.76	
	AST3A1 030903050914120613002 4l	20030903	34.83	84.62	
	*AST3A1 011116051347120615005 5l	20011116	35.91	84.78	
	AST3A1 011116051356120615005 4l	20011116	35.38	84.64	
	AST3A1 011116051405120613002 2l	20011116	34.85	84.49	
	AST3A1 010328052626120615000 8l	20010328	35.75	84.39	
	AST3A1 010328052635150716000l	20010328	35.22	84.24	
	*AST3A1 071115052131120615000 7l	20071115	36.09	84.26	
	AST3A1 071115052140120615000 5l	20071115	35.56	84.09	
	AST3A1 071115052148150716000l	20071115	35.03	83.93	
	AST3A1 031028051557150715000l	20031028	35.10	85.07	
	AST3A1 070414051613120613002 9l	20070414	35.22	84.25	
	AST3A1 080228051558120613003 3l	20080228	35.27	83.93	
(36°N, 85°E)	AST3A1 020916051109150716000l	20020916	35.70	86.27	13(5), 0(0)
	*AST3A1 030903050906120615005 6l	20030903	35.37	84.79	
	*AST3A1 031028051539120615005 1l	20031028	36.16	85.38	
	AST3A1 031028051548120615000 3l	20031028	35.63	85.22	
	*AST3A1 030903050857120615005 3l	20030903	35.90	84.91	
	AST3A1 021002051109150716000l	20021002	34.69	85.65	
	*AST3A1 001104052900150313000 1l	20001104	36.10	85.74	
	AST3A1 001104052918150716000l	20001104	35.04	85.42	
	AST3A1 001215052207150313000 1l	20001215	36.28	86.12	
	AST3A1 001215052216150313000 1l	20001215	35.75	85.96	
	AST3A1 001215052225150313000 1l	20001215	35.22	85.81	
	*AST3A1 031028051557150715000l	20031028	35.10	85.07	
	AST3A1 071226051553150730000l	20071226	35.57	85.58	
(36°N, 86°E)	*AST3A1 001028052302150714000l	20001028	36.11	87.26	11(5), 0(0)
	AST3A1 001028052311150714000l	20001028	35.58	87.10	
	AST3A1 001028052320150714000l	20001028	35.05	86.94	
	AST3A1 010711051744150714000l	20010711	35.64	86.66	
	*AST3A1 020916051109150716000l	20020916	35.70	86.27	
	*AST3A1 030802050837150717000l	20030802	36.26	86.21	
	*AST3A1 001215052216150313000 1l	20001215	35.75	85.96	
	*AST3A1 001215052225150313000 1l	20001215	35.22	85.81	
	AST3A1 041023050826150717000l	20041023	36.17	86.82	
	AST3A1 041023050844150313000 1l	20041023	35.11	86.51	
	AST3A1 070306051009150313000 1l	20070306	35.17	86.15	
(36°N, 87°E)	AST3A1 011024050834150717000l	20011024	36.29	87.55	12(6), 0(0)
	*AST3A1 011024050843150714000l	20011024	35.76	87.39	
	AST3A1 011024050852150714000l	20011024	35.23	87.24	
	*AST3A1 001028052302150714000l	20001028	36.11	87.26	

	*AST3A1 0010280523111507140001	20001028	35.58	87.10	
	*AST3A1 0010280523201507140001	20001028	35.05	86.94	
	*AST3A1 0403310457161507140001	20040331	35.85	88.34	
	AST3A1 0709160457391507140001	20070916	35.34	88.04	
	AST3A1 0709160457481504130001	20070916	34.81	87.90	
	*AST3A1 0510280456251507140001	20051028	35.92	87.82	
	AST3A1 0510280456341507140001	20051028	35.39	87.68	
	AST3A1 0510280456431504130001	20051028	34.86	87.53	
(36°N, 88°E)	*AST3A1 0403310457161507140001	20040331	35.85	88.34	10(4), 0(0)
	AST3A1 0403310457251507140001	20040331	35.32	88.20	
	AST3A1 0403310457341507140001	20040331	34.79	88.05	
	*AST3A1 0204110458281507140001	20020411	35.80	88.73	
	AST3A1 0204110458361507140001	20020411	35.26	88.58	
	AST3A1 0204110458451507140001	20020411	34.73	88.43	
	*AST3A1 0110100456491507140001	20011010	35.93	89.32	
	AST3A1 0110100456581507140001	20011010	35.40	89.18	
	AST3A1 0110100457061507140001	20011010	34.86	89.03	
	*AST3A1 0307190456311507140001	20030719	35.90	87.97	
(36°N, 89°E)	*AST3A1 0309210456421507140001	20030921	36.15	90.06	8(5), 2(0)
	AST3A1 0309210457001507140001	20030921	35.09	89.75	
	AST3A1 0205130458481507140001	20020513	35.58	90.19	
	AST3A1 0309210456511507140001	20030921	35.62	89.90	
	*AST3A1 0110100456491507140001	20011010	35.93	89.32	
	*AST3A1 0110100456581507140001	20011010	35.40	89.18	
	*AST3A1 0110100457061507140001	20011010	34.86	89.03	
	*AST3A1 0204110458281507140001	20020411	35.80	88.73	
	ASTL1B 0110100456490804080030	20011010	35.93	89.32	
	ASTL1B 0110100456580804230769	20011010	35.40	89.18	
(35°N, 84°E)	AST3A1 0011040529271206130018	20001104	34.52	85.26	16(4), 0(0)
	AST3A1 0011040529351206130050	20001104	33.99	85.10	
	*AST3A1 0111160514051206130022	20011116	34.85	84.49	
	AST3A1 0111160514141206130052	20011116	34.32	84.35	
	AST3A1 0111160514231206130053	20011116	33.79	84.28	
	AST3A1 0611210515251206130056	20061121	35.21	84.29	
	AST3A1 0611210515341206130023	20061121	34.68	84.14	
	AST3A1 0611210515421206130003	20061121	34.15	83.99	
	*AST3A1 0309030509141206130024	20030903	34.83	84.62	
	AST3A1 0309030509231206130027	20030903	34.30	84.48	
	AST3A1 0706100510041206130026	20070610	34.26	84.79	
	AST3A1 0706100510131206130011	20070610	33.73	84.65	
	*AST3A1 0310280515571507150001	20031028	35.10	85.07	
	AST3A1 0310280516061206130025	20031028	34.57	84.91	
	AST3A1 0612230515581206130007	20061223	34.13	84.18	
	*AST3A1 0103280526351507160001	20010328	35.22	84.24	
(35°N, 85°E)	AST3A1 0409050509261507150001	20040905	34.11	85.85	11(5), 0(0)
	AST3A1 0404050515481507150001	20040405	35.03	85.51	
	*AST3A1 0703060510091503130001	20070306	35.17	86.15	
	AST3A1 0703060510181503130001	20070306	34.64	86.00	
	*AST3A1 0011040529181507160001	20001104	35.04	85.42	
	*AST3A1 0011040529271206130018	20001104	34.52	85.26	
	*AST3A1 0011040529351206130050	20001104	33.99	85.10	
	AST3A1 0812050510281507150001	20081205	34.68	85.68	
	AST3A1 0812050510371507150001	20081205	34.15	85.53	
	*AST3A1 0310280515571507150001	20031028	35.10	85.07	
	AST3A1 0310280516061206130025	20031028	34.57	84.91	
(35°N, 86°E)	*AST3A1 0010280523201507140001	20001028	35.05	86.94	9(4), 0(0)
	AST3A1 0010280523281503130001	20001028	34.52	86.78	
	AST3A1 0010280523371503100001	20001028	33.99	86.63	

	AST3A1 011024050910150310001	20011024	34.17	86.95	
	*AST3A1 041023050844150313001	20041023	35.11	86.51	
	AST3A1 041023050853150313001	20041023	34.58	86.35	
	AST3A1 041023050902150313001	20041023	34.05	86.20	
	*AST3A1 070306051009150313001	20070306	35.17	86.15	
	*AST3A1 070306051018150313001	20070306	34.64	86.00	
(35°N, 87°E)	*AST3A1 001028052320150714001	20001028	35.05	86.94	14(5), 0(0)
	*AST3A1 001028052328150313001	20001028	34.52	86.78	
	*AST3A1 001028052337150310001	20001028	33.99	86.63	
	*AST3A1 051028045643150413001	20051028	34.86	87.53	
	AST3A1 051028045652150413001	20051028	34.33	87.39	
	AST3A1 051028045701150413001	20051028	33.79	87.25	
	AST3A1 011008050928150413001	20011008	34.53	88.26	
	AST3A1 011008050937150413001	20011008	34.00	88.10	
	AST3A1 051120050248150413001	20051120	35.24	87.23	
	AST3A1 051120050257150413001	20051120	34.71	87.08	
	AST3A1 051120050306150413001	20051120	34.17	86.93	
	*AST3A1 070916045748150413001	20070916	34.81	87.90	
	AST3A1 070916045757150413001	20070916	34.28	87.75	
	AST3A1 070916045806150720001	20070916	33.75	87.60	
(35°N, 88°E)	AST3A1 011008050919150413001	20011008	35.06	88.41	9(4), 0(0)
	*AST3A1 011008050928150413001	20011008	34.52	86.78	
	*AST3A1 011008050937150413001	20011008	33.99	86.63	
	AST3A1 001030051100150714001	20001030	34.69	88.74	
	AST3A1 001030051109150714001	20001030	34.16	88.59	
	*AST3A1 011010045706150714001	20011010	34.86	89.03	
	AST3A1 011010045715150714001	20011010	34.33	88.89	
	AST3A1 011010045724150714001	20011010	33.80	88.75	
	*AST3A1 040331045734150714001	20040331	34.79	88.05	
(35°N, 89°E)	*AST3A1 030921045700150714001	20030921	35.09	89.75	9(4), 0(0)
	AST3A1 030921045709150714001	20030921	34.56	89.59	
	AST3A1 020513045857150714001	20020513	35.05	90.03	
	AST3A1 020513045906150714001	20020513	34.52	89.87	
	*AST3A1 011010045706150714001	20011010	34.86	89.03	
	*AST3A1 011010045715150714001	20011010	34.33	88.89	
	*AST3A1 011010045724150714001	20011010	33.80	88.75	
	AST3A1 001007050531150720001	20001007	34.17	90.09	
	AST3A1 030921045717150720001	20030921	34.03	89.43	
(34°N, 84°E)	AST3A1 040507051621120613005	20040507	34.05	84.71	9(2), 0(0)
	AST3A1 040507051630120613004	20040507	33.52	84.56	
	AST3A1 040507051639120612016	20040507	32.99	84.40	
	*AST3A1 001104052935120613050	20001104	33.99	85.10	
	AST3A1 001104052944120613051	20001104	33.46	84.95	
	AST3A1 001104052953150424001	20001104	32.93	84.80	
	*AST3A1 011116051423120613053	20011116	33.79	84.21	
	AST3A1 011116051432120612049	20011116	33.26	84.07	
	AST3A1 011116051440120612015	20011116	32.72	83.94	
(34°N, 85°E)	*AST3A1 040905050926150715001	20040905	34.11	85.85	10(4), 0(0)
	AST3A1 040905050935150715001	20040905	33.58	85.70	
	AST3A1 040905050944150309001	20040905	33.05	85.55	
	*AST3A1 001104052935120613050	20001104	33.99	85.10	
	*AST3A1 001104052944120613051	20001104	33.46	84.95	
	AST3A1 041023050911150715001	20041023	33.52	86.04	
	AST3A1 041023050919150309001	20041023	32.99	85.89	
	*AST3A1 081205051037150715001	20081205	34.15	85.53	
	AST3A1 081205051046120613014	20081205	33.62	85.38	
	AST3A1 081205051055150424001	20081205	33.09	85.23	
(34°N, 86°E)	*AST3A1 040905050926150715001	20040905	34.11	85.85	13(7), 0(0)

	*AST3A1 040905050935150715 0001	20040905	33.58	85.70	
	*AST3A1 041023050902150313 0001	20041023	34.05	86.20	
	*AST3A1 041023050911150715 0001	20041023	33.52	86.04	
	*AST3A1 041023050919150309 0001	20041023	32.99	85.89	
	*AST3A1 001028052337150310 0001	20001028	33.99	86.63	
	AST3A1 001028052346150310 0001	20001028	33.46	86.47	
	AST3A1 001028052355150309 0001	20001028	32.93	86.32	
	*AST3A1 011024050910150310 0001	20011024	34.17	86.95	
	AST3A1 011024050919150310 0001	20011024	33.64	86.80	
	AST3A1 011024050928150309 0001	20011024	33.11	86.65	
	AST3A1 051028045710150309 0001	20051028	33.26	87.11	
	AST3A1 051028045718150309 0001	20051028	32.73	86.97	
(34°N, 87°E)	*AST3A1 011008050937150413 0001	20011008	34.00	88.10	16(9), 0(0)
	*AST3A1 011024050910150310 0001	20011024	34.17	86.95	
	*AST3A1 011024050919150310 0001	20011024	33.64	86.80	
	*AST3A1 011024050928150309 0001	20011024	33.11	86.65	
	AST3A1 020411045912150415 0001	20020411	33.14	87.99	
	*AST3A1 051028045701150413 0001	20051028	33.79	87.25	
	*AST3A1 051028045710150309 0001	20051028	33.26	87.11	
	*AST3A1 051028045718150309 0001	20051028	32.73	86.97	
	AST3A1 011008050954150710 0001	20011008	32.94	87.80	
	AST3A1 070308045805150710 0001	20070308	34.22	88.18	
	AST3A1 070308045814150710 0001	20070308	33.69	88.04	
	AST3A1 070308045823150415 0001	20070308	33.15	87.89	
	AST3A1 070916045815150415 0001	20070916	33.21	87.47	
	*AST3A1 070916045757150413 0001	20070916	34.28	87.75	
	AST3A1 011008050945150710 0001	20011008	33.47	87.95	
	*AST3A1 070916045806150730 0001	20070916	33.75	87.60	
(34°N, 88°E)	*AST3A1 070308045805150710 0001	20070308	34.22	88.18	11(6), 0(0)
	*AST3A1 070308045814150710 0001	20070308	33.69	88.04	
	*AST3A1 070308045823150415 0001	20070308	33.15	87.89	
	AST3A1 030921045726150710 0001	20030921	33.50	89.28	
	AST3A1 030921045735150710 0001	20030921	32.97	89.13	
	*AST3A1 011010045724150714 0001	20011010	33.80	88.75	
	AST3A1 011010045733150701 0001	20011010	33.27	88.61	
	AST3A1 011010045742150701 0001	20011010	32.74	88.48	
	*AST3A1 020411045912150415 0001	20020411	33.14	87.99	
	*AST3A1 001030051109150714 0001	20001030	34.16	88.59	
	AST3A1 001030051118150710 0001	20001030	33.63	88.44	
(34°N, 89°E)	*AST3A1 030921045726150710 0001	20030921	33.50	89.28	9(6), 0(0)
	*AST3A1 030921045735150710 0001	20030921	32.97	89.13	
	*AST3A1 011010045724150714 0001	20011010	33.80	88.75	
	*AST3A1 011010045733150701 0001	20011010	33.27	88.61	
	AST3A1 001007050548150707 0001	20001007	33.10	89.80	
	AST3A1 010814050543150707 0001	20010814	32.96	89.24	
	*AST3A1 001007050531150730 0001	20001007	34.17	90.09	
	AST3A1 001007050540150730 0001	20001007	33.63	89.95	
	*AST3A1 030921045717150730 0001	20030921	34.03	89.43	
(33°N, 84°E)	*AST3A1 040507051639120612 0016	20040507	32.99	84.40	10(4), 0(0)
	AST3A1 040507051647120612 0018	20040507	32.46	84.26	
	AST3A1 040507051656120612 0019	20040507	31.93	84.11	
	*AST3A1 001104052953150424 0001	20001104	32.93	84.80	
	AST3A1 001104053002120612 0046	20001104	32.40	84.64	
	AST3A1 001104053011120612 0041	20001104	31.87	84.49	
	*AST3A1 011116051432120612 0049	20011116	33.26	84.07	
	*AST3A1 011116051440120612 0015	20011116	32.72	83.94	
	AST3A1 021002051144150424 0001	20021002	32.57	85.06	
	AST3A1 021002051153150424 0001	20021002	32.04	84.91	

(33°N, 85°E)	*AST3A1 040905050944150309001	20040905	33.05	85.55	11(4), 0(0)
	AST3A1 04090505095315042400	20040905	32.52	85.40	
	AST3A1 04090505100215042400	20040905	31.98	85.26	
	*AST3A1 001104052953150424000	20001104	32.93	84.80	
	*AST3A1 0011040530021206120046	20001104	32.40	84.64	
	AST3A1 031014050409150309001	20031014	33.20	86.04	
	AST3A1 031014050418150309001	20031014	32.67	85.89	
	AST3A1 031014050427150424000	20031014	32.14	85.75	
	AST3A1 021002051135150424000	20021002	33.10	85.20	
	AST3A1 081205051103150424000	20081205	32.56	85.09	
	*AST3A1 021002051153150424000	20021002	32.04	84.91	
(33°N, 86°E)	*AST3A1 011024050928150309001	20011024	33.11	86.65	10(4), 0(0)
	AST3A1 01102405094515020600	20011024	32.05	86.37	
	*AST3A1 001028052355150309000	20001028	32.93	86.32	
	AST3A1 001028052404150309000	20001028	32.40	86.17	
	AST3A1 001028052413150206000	20001028	31.87	86.02	
	AST3A1 061031045729150309000	20061031	32.71	87.10	
	AST3A1 061031045737150206000	20061031	32.18	86.96	
	*AST3A1 031014050409150309001	20031014	33.20	86.04	
	*AST3A1 031014050418150309001	20031014	32.67	85.89	
	AST3A1 011024050936150730000	20011024	32.58	86.51	
(33°N, 87°E)	AST3A1 001030051127150701000	20001030	33.10	88.30	14(5), 4(0)
	AST3A1 00103005113615070100	20001030	32.57	88.15	
	AST3A1 00103005114415070100	20001030	32.03	88.01	
	*AST3A1 020411045912150415000	20020411	33.14	87.99	
	AST3A1 02041104592115041500	20020411	32.61	87.85	
	AST3A1 02041104592915041500	20020411	32.08	87.71	
	*AST3A1 061031045729150309000	20061031	32.71	87.10	
	*AST3A1 061031045737150206000	20061031	32.18	86.96	
	*AST3A1 070308045823150415000	20070308	33.15	87.89	
	AST3A1 07030804583215041500	20070308	32.62	87.75	
	AST3A1 07030804584115041500	20070308	32.09	87.61	
	*AST3A1 051028045710150309000	20051028	33.26	87.11	
	AST3A1 020310045925150415000	20020310	33.20	87.56	
	AST3A1 080214050434150206000	20080214	31.92	87.23	
	ASTL1B 061031045729080513001	20061031	32.71	87.10	
	ASTL1B 06103104573707100200	20061031	32.18	86.96	
	ASTL1B 07030804583207103000	20070308	32.62	87.75	
	ASTL1B 07030804584107100200	20070308	32.09	87.61	
(33°N, 88°E)	*AST3A1 010814050543150707000	20010814	32.96	89.24	10(6), 0(0)
	*AST3A1 001030051127150701000	20001030	33.10	88.30	
	*AST3A1 00103005113615070100	20001030	32.57	88.15	
	*AST3A1 00103005114415070100	20001030	32.03	88.01	
	AST3A1 061008045108150701000	20061008	33.19	89.19	
	AST3A1 061008045117150701000	20061008	32.66	89.05	
	AST3A1 061008045126150701000	20061008	32.13	88.91	
	*AST3A1 011010045733150701000	20011010	33.27	88.61	
	*AST3A1 011010045742150701000	20011010	32.74	88.48	
	AST3A1 01101004575115070100	20011010	32.20	88.34	
(33°N, 89°E)	*AST3A1 001007050548150707000	20001007	33.10	89.80	8(2), 0(0)
	AST3A1 00100705055715070700	20001007	32.57	89.65	
	AST3A1 00100705060615070700	20001007	32.04	89.51	
	AST3A1 001101045906150707000	20001101	32.75	90.14	
	AST3A1 00110104591515070700	20001101	32.19	90.01	
	*AST3A1 010814050543150707000	20010814	32.96	89.24	
	AST3A1 010814050552150707000	20010814	32.43	89.09	
	AST3A1 010814050601150707000	20010814	31.90	88.94	
(32°N, 84°E)	*AST3A1 021002051153150424000	20021002	32.04	84.91	10(3), 0(0)

	AST3A1 021002051202120618005 9	20021002	31.50	84.77	
	AST3A1 021002051210150710000 1	20021002	30.97	84.63	
	*AST3A1 001104053011120612004 1	20001104	31.87	84.49	
	AST3A1 001104053020120618006 0	20001104	31.34	84.35	
	AST3A1 001104053028090722050 2	20001104	30.81	84.20	
	*AST3A1 040507051656120612001 9	20040507	31.93	84.11	
	AST3A1 040507051705120618005 6	20040507	31.39	83.95	
	AST3A1 080104051104150713000 1	20080104	30.92	85.01	
	AST3A1 080104051055150713000 1	20080104	31.45	85.15	
(32°N, 85°E)	*AST3A1 011024050945150206000 1	20011024	32.05	86.37	13(4), 0(0)
	AST3A1 011024050954150206000 1	20011024	31.52	86.22	
	*AST3A1 021002051153150424000 1	20021002	32.04	84.91	
	AST3A1 030304050524150709000 1	20030304	30.96	86.24	
	AST3A1 071101051023150206000 1	20071101	31.92	85.70	
	AST3A1 071101051041120618001 0	20071101	30.86	85.40	
	AST3A1 080301050437150206000 1	20080301	31.55	86.01	
	AST3A1 111128051015150206000 1	20111128	31.32	85.97	
	AST3A1 111128051024150206000 1	20111128	30.79	85.82	
	AST3A1 070306051102150424000 1	20070306	31.99	85.25	
	*AST3A1 080104051104150713000 1	20080104	30.92	85.01	
	*AST3A1 080104051055150713000 1	20080104	31.45	85.15	
	AST3A1 040313051113150713000 1	20040313	31.40	85.50	
(32°N, 86°E)	*AST3A1 071101051023150206000 1	20071101	31.92	85.70	9(3), 0(0)
	AST3A1 020222045959150206000 1	20020222	32.20	86.86	
	AST3A1 020222050008150206000 1	20020222	31.66	86.73	
	AST3A1 020222050017150206000 1	20020222	31.13	86.59	
	*AST3A1 011024050945150206000 1	20011024	32.05	86.37	
	*AST3A1 011024050954150206000 1	20011024	31.52	86.22	
	AST3A1 011024051003150206000 1	20011024	30.99	86.08	
	AST3A1 020310045951150206000 1	20020310	31.61	87.15	
	AST3A1 020310050000150206000 1	20020310	31.07	87.01	
(32°N, 87°E)	*AST3A1 001030051144150701000 1	20001030	32.03	88.01	13(3), 0(0)
	*AST3A1 020411045929150415000 1	20020411	32.08	87.71	
	AST3A1 060224050349150206000 1	20060224	30.85	86.98	
	AST3A1 020310045943150206000 1	20020310	32.14	87.28	
	AST3A1 080310045820150206000 1	20080310	31.60	87.22	
	AST3A1 080310045829150206000 1	20080310	31.06	87.08	
	*AST3A1 080214050434150206000 1	20080214	31.92	87.23	
	AST3A1 021004045945150708000 1	20021004	31.02	87.37	
	AST3A1 011010045800150708000 1	20011010	31.67	88.20	
	AST3A1 011010045808150708000 1	20011010	31.14	88.07	
	AST3A1 001030051202150730000 1	20001030	30.97	87.73	
	AST3A1 001030051153150730000 1	20001030	31.50	87.87	
	AST3A1 080207045834150730000 1	20080207	31.55	87.52	
(32°N, 88°E)	*AST3A1 011010045751150701000 1	20011010	32.20	88.34	9(3), 0(0)
	*AST3A1 011010045800150708000 1	20011010	31.67	88.20	
	*AST3A1 011010045808150708000 1	20011010	31.14	88.07	
	AST3A1 071103045759150708000 1	20071103	31.92	88.80	
	AST3A1 071103045808150708000 1	20071103	31.39	88.65	
	AST3A1 071103045817150708000 1	20071103	30.86	88.51	
	AST3A1 020105050106150708000 1	20020105	31.87	89.10	
	AST3A1 020105050114150708000 1	20020105	31.34	88.95	
	AST3A1 020105050123150708000 1	20020105	30.81	88.80	
(32°N, 89°E)	*AST3A1 071103045759150708000 1	20071103	31.92	88.80	10(3), 0(0)
	*AST3A1 071103045808150708000 1	20071103	31.39	88.65	
	*AST3A1 001101045915150707000 1	20001101	32.19	90.01	
	AST3A1 001101045924150709000 1	20001101	31.66	89.87	
	AST3A1 040301044648150708000 1	20040301	31.08	90.04	

	AST3A1 020215045350150709001	20020215	31.44	89.81	
	AST3A1 020215045359150708001	20020215	30.91	89.67	
	AST3A1 011127045618150709001	20011127	32.05	89.46	
	AST3A1 011127045627150709001	20011127	31.52	89.32	
	AST3A1 011127045636150709001	20011127	30.99	89.18	
(31°N, 84°E)	AST3A1 071101051049120426004	20071101	30.33	85.26	12(2), 0(0)
	AST3A1 071101051058120426004	20071101	29.80	85.12	
	*AST3A1 080104051104150713001	20080104	30.92	85.01	
	AST3A1 001215052335120615002	20001215	30.97	84.65	
	AST3A1 070117051102150710001	20070117	30.92	85.00	
	AST3A1 070117051110150710001	20070117	30.39	84.85	
	AST3A1 070117051119100416002	20070117	29.86	84.71	
	AST3A1 021002051219150710001	20021002	30.44	84.49	
	AST3A1 021002051228100414050	20021002	29.91	84.35	
	*AST3A1 001104053028090722050	20001104	30.81	84.20	
	AST3A1 001104053037090722050	20001104	30.27	84.05	
	AST3A1 001104053046090722050	20001104	29.74	83.91	
(31°N, 85°E)	*AST3A1 030304050524150709001	20030304	30.96	86.24	11(6), 0(0)
	AST3A1 030304050533150709001	20030304	30.43	86.10	
	AST3A1 030304050542120501002	20030304	29.90	85.96	
	*AST3A1 071101051041120618001	20071101	30.86	85.40	
	*AST3A1 071101051049120426004	20071101	30.33	85.26	
	*AST3A1 071101051058120426004	20071101	29.80	85.12	
	AST3A1 040313051130120615002	20040313	30.33	85.21	
	AST3A1 080301050455150709001	20080301	30.48	85.75	
	AST3A1 080301050503120426005	20080301	29.95	85.59	
	*AST3A1 111128051024150206001	20111128	30.79	85.82	
	*AST3A1 080104051104150713001	20080104	30.92	85.01	
(31°N, 86°E)	AST3A1 040923045755150206001	20040923	31.07	87.02	10(4), 0(0)
	AST3A1 040923045804150414001	20040923	30.54	86.88	
	*AST3A1 020222050017150206001	20020222	31.13	86.59	
	AST3A1 020222050026150414001	20020222	30.60	86.46	
	AST3A1 020222050035120426004	20020222	30.07	86.32	
	*AST3A1 030304050524150709001	20030304	30.96	86.24	
	*AST3A1 030304050533150709001	20030304	30.43	86.10	
	*AST3A1 030304050542120501002	20030304	29.90	85.96	
	AST3A1 001115051214120502002	20001115	30.02	86.69	
	AST3A1 021004050002150708001	20021004	29.96	87.10	
(31°N, 87°E)	*AST3A1 011010045808150708001	20011010	31.14	88.07	10(5), 0(0)
	AST3A1 011010045817150708001	20011010	30.61	87.94	
	AST3A1 011010045826120508002	20011010	30.08	87.80	
	AST3A1 001030051211150708001	20001030	30.44	87.59	
	AST3A1 001030051220120508001	20001030	29.91	87.45	
	*AST3A1 040923045755150206001	20040923	31.07	87.02	
	*AST3A1 021004045945150708001	20021004	31.02	87.37	
	AST3A1 021004045953150708001	20021004	30.49	87.23	
	*AST3A1 021004050002150708001	20021004	29.96	87.10	
	*AST3A1 001030051202150720001	20001030	30.97	87.73	
(31°N, 88°E)	AST3A1 011213045549150708001	20011213	30.98	89.24	12(4), 0(0)
	AST3A1 011213045558150708001	20011213	30.44	89.10	
	AST3A1 011213045607120509002	20011213	29.91	88.96	
	AST3A1 091016045225150708001	20091016	31.07	88.58	
	AST3A1 091016045234150708001	20091016	30.54	88.44	
	AST3A1 091016045243120508004	20091016	30.01	88.30	
	*AST3A1 011010045808150708001	20011010	31.14	88.07	
	*AST3A1 011010045817150708001	20011010	30.61	87.94	
	*AST3A1 011010045826150708001	20011010	30.08	87.80	
	*AST3A1 020105050123150708001	20020105	30.81	88.80	

	AST3A1 020105050132120509002	20020105	30.28	88.66	
	AST3A1 020105050141030302109 1	20020105	29.75	88.51	
(31°N, 89°E)	*AST3A1 011213045549150708001	20011213	30.98	89.24	9(5), 0(0)
	*AST3A1 011213045558150708001	20011213	30.44	89.10	
	*AST3A1 011213045607120509002	20011213	29.91	88.96	
	*AST3A1 020215045359150708001	20020215	30.91	89.67	
	AST3A1 020215045408150708001	20020215	30.38	89.53	
	AST3A1 020215045417120511001 6	20020215	29.85	89.39	
	*AST3A1 040301044648150708001	20040301	31.08	90.04	
	AST3A1 040301044657150708001	20040301	30.55	89.90	
	AST3A1 040301044706120511000 2	20040301	30.02	89.77	
(30°N, 84°E)	AST3A1 001129052408120605006 4	20001129	29.91	84.38	11(2), 0(0)
	AST3A1 021002051237100414050 8	20021002	29.38	84.21	
	*AST3A1 001104053046090722050 4	20001104	29.74	83.91	
	AST3A1 041117050347120605002 5	20041117	30.00	85.22	
	*AST3A1 041117050356120605003 2	20041117	29.47	85.09	
	AST3A1 070117051119100416002 0	20070117	29.86	84.71	
	AST3A1 070117051128100416002 1	20070117	29.32	84.57	
	AST3A1 041023051030120605000 4	20041023	28.75	84.74	
	AST3A1 041101050415120605000 5	20041101	28.95	84.87	
	AST3A1 031005051125100414051 6	20031005	28.84	84.12	
	AST3A1 111011051104120427001 5	20111011	28.78	84.49	
(30°N, 85°E)	*AST3A1 041117050356120605003 2	20041117	29.47	85.09	8(2), 0(0)
	*AST3A1 041117050347120605002 5	20041117	30.00	85.22	
	AST3A1 001028052457090722050 1	20001028	29.22	85.29	
	AST3A1 031030050502120426000 3	20031030	29.90	85.95	
	AST3A1 031030050511120426000 4	20031030	29.37	85.81	
	AST3A1 031030050520120420003 5	20031030	28.84	85.67	
	AST3A1 020204051312120426003 8	20020204	30.28	85.54	
	AST3A1 001028052448120605002 7	20001028	29.75	85.43	
(30°N, 86°E)	*AST3A1 031030050520120420003 5	20031030	28.84	85.67	12(4), 0(0)
	*AST3A1 031030050511120426000 4	20031030	29.37	85.81	
	*AST3A1 031030050502120426000 3	20031030	29.90	85.95	
	AST3A1 041110045801120420000 7	20041110	28.87	86.99	
	AST3A1 041110045752120502000 2	20041110	29.40	87.12	
	AST3A1 041110045743120502000 2	20041110	29.93	87.26	
	*AST3A1 001115051214120502000 2	20001115	30.02	86.69	
	AST3A1 001115051223120502000 3	20001115	28.95	86.42	
	AST3A1 001115051232120420000 2	20001115	29.48	86.55	
	AST3A1 040502045858120426000 4	20040502	30.06	86.37	
	AST3A1 040502045907120426000 3	20040502	29.53	86.23	
	AST3A1 040502045916120420003 2	20040502	29.00	86.10	
(30°N, 87°E)	*AST3A1 041110045752120502000 2	20041110	29.40	87.12	12(4), 0(0)
	*AST3A1 041110045743120502000 2	20041110	29.93	87.26	
	AST3A1 031023045911120420001 1	20031023	28.84	87.21	
	AST3A1 031023045902120502000 8	20031023	29.37	87.34	
	*AST3A1 001030051220120508001 9	20001030	29.91	87.45	
	AST3A1 071103045852120508002 0	20071103	28.73	87.94	
	AST3A1 071103045843120508002 1	20071103	29.26	88.08	
	AST3A1 071103045834120508002 5	20071103	29.79	88.22	
	*AST3A1 011010045826120508002 7	20011010	30.08	87.80	
	AST3A1 091108045905120508002 6	20091108	29.85	87.81	
	AST3A1 091108045913120508002 3	20091108	29.32	87.67	
	AST3A1 091108045922120508002 2	20091108	28.79	87.53	
(30°N, 88°E)	AST3A1 011127045712150727000 1	20011127	28.86	88.62	11(3), 0(0)
	AST3A1 011127045703150727000 1	20011127	29.39	88.76	
	AST3A1 011127045654120509000 2	20011127	29.92	88.90	
	AST3A1 021029045410150727000 1	20021029	28.90	88.35	

	AST3A1 021029045401150727 0001	20021029	29.43	88.48	
	AST3A1 001201051139150727 0001	20001201	29.74	88.58	
	AST3A1 011111045726150727 0001	20011111	28.95	87.98	
	*AST3A1 011010045826120508 0027	20011010	30.08	87.80	
	*AST3A1 071103045843120508 0021	20071103	29.26	88.08	
	*AST3A1 071103045834120508 0025	20071103	29.79	88.22	
	AST3A1 001101050008150727 0001	20001101	28.99	89.21	
(30°N, 89°E)	*AST3A1 001101050008150727 0001	20001101	28.99	89.21	10(3), 0(0)
	AST3A1 040301044724150727 0001	20040301	28.95	89.50	
	AST3A1 051208045159120511 0009	20051208	29.23	89.81	
	AST3A1 051224045147120511 0002	20051224	29.22	89.90	
	AST3A1 051208045150120511 0002	20051208	29.77	89.95	
	*AST3A1 040301044706120511 0002	20040301	30.02	89.77	
	AST3A1 040301044715150727 0001	20040301	29.48	89.63	
	AST3A1 031110044703150727 0001	20031110	29.53	89.28	
	AST3A1 031110044654120511 0002	20031110	30.07	89.41	
	*AST3A1 011127045654120509 0002	20011127	29.92	88.90	
(29°N, 84°E)	AST3A1 120303051150120510 0017	20120303	27.68	84.50	15(1), 0(0)
	AST3A1 001028052506090721 0629	20001028	28.69	85.14	
	AST3A1 001215052411100414 0500	20001215	28.84	84.09	
	*AST3A1 111011051104120427 0015	20111011	28.78	84.49	
	AST3A1 041023051021120501 0018	20041023	29.28	84.88	
	AST3A1 071101051116120426 0046	20071101	28.73	84.83	
	AST3A1 041101050433120510 0009	20041101	27.89	84.61	
	AST3A1 051104050451120510 0028	20051104	27.89	84.57	
	AST3A1 031122051230120510 0011	20031122	28.17	84.88	
	AST3A1 041101050424120510 0016	20041101	28.42	84.74	
	AST3A1 040210051233120510 0014	20040210	27.79	83.74	
	AST3A1 040210051224120510 0010	20040210	28.32	83.87	
	AST3A1 080409051146120510 0039	20080409	27.77	83.91	
	AST3A1 080104051148120510 0011	20080104	28.26	84.31	
	AST3A1 010305052302120510 0025	20010305	27.73	84.15	
(29°N, 85°E)	*AST3A1 001028052506090721 0629	20001028	28.69	85.14	11(4), 0(0)
	*AST3A1 001028052457090722 0501	20001028	29.22	85.29	
	AST3A1 041203050428120510 0021	20041203	27.87	84.70	
	AST3A1 041228045841120420 0002	20041228	27.93	85.84	
	AST3A1 041228045832120420 0002	20041228	28.46	85.97	
	AST3A1 041228045823120420 0004	20041228	29.00	86.10	
	*AST3A1 031122051230120510 0011	20031122	28.17	84.88	
	*AST3A1 031030050520120420 0035	20031030	28.84	85.67	
	AST3A1 050221050445120511 0076	20050221	27.76	85.46	
	AST3A1 071117051123120510 0013	20071117	28.14	85.08	
	AST3A1 031030050529120511 0074	20031030	28.31	85.54	
(29°N, 86°E)	AST3A1 051113045841120420 0002	20051113	27.79	86.80	10(5), 0(0)
	*AST3A1 001115051232120420 0002	20001115	28.95	86.42	
	AST3A1 001115051241120420 0002	20001115	28.42	86.29	
	*AST3A1 041228045841120420 0002	20041228	27.93	85.84	
	*AST3A1 041228045832120420 0002	20041228	28.46	85.97	
	*AST3A1 041228045823120420 0004	20041228	29.00	86.10	
	AST3A1 041110045819120420 0008	20041110	27.81	86.72	
	AST3A1 041110045810120420 0005	20041110	28.34	86.85	
	*AST3A1 041110045801120420 0007	20041110	28.87	86.99	
	AST3A1 051206050439120420 0002	20051206	28.17	86.42	
(29°N, 87°E)	AST3A1 031023045929120420 0003	20031023	27.77	86.93	10(1), 0(0)
	AST3A1 011220050211120420 0042	20011220	28.84	87.21	
	AST3A1 011220050220120420 0045	20011220	29.37	87.34	
	AST3A1 020105050159150727 0001	20020105	28.69	88.23	
	AST3A1 020105050207120514 0002	20020105	28.16	88.09	

	AST3A1 001124050626120514 0002	20001124	27.93	87.36	
	*AST3A1 071103045852120508 0020	20071103	28.73	87.94	
	AST3A1 071103045901120514 0002	20071103	28.20	87.80	
	AST3A1 071221045914120508 0048	20071221	28.79	87.54	
	AST3A1 071221045922120423 0014	20071221	28.26	87.41	
(29°N, 88°E)	*AST3A1 011127045712150727 0001	20011127	28.86	88.62	9(4), 0(0)
	AST3A1 020105050150150727 0001	20020105	29.22	88.37	
	*AST3A1 020105050159150727 0001	20020105	28.69	88.23	
	AST3A1 011213045633120515 0009	20011213	28.32	88.55	
	AST3A1 011213045642120514 0009	20011213	27.78	88.42	
	*AST3A1 001101050008150727 0001	20001101	28.99	89.21	
	AST3A1 001101050017120515 0010	20001101	28.46	89.08	
	AST3A1 001101050026120515 0003	20001101	27.93	88.95	
	*AST3A1 020105050207120514 0002	20020105	28.16	88.09	
(29°N, 89°E)	AST3A1 011120045121120515 0047	20011120	27.79	89.94	13(6), 0(0)
	*AST3A1 051208045159120511 0009	20051208	29.23	89.81	
	*AST3A1 051224045147120511 0002	20051224	29.22	89.90	
	AST3A1 041103045154120511 0041	20041103	28.69	89.76	
	AST3A1 011120045112120515 0046	20011120	28.32	90.07	
	*AST3A1 001101050008150727 0001	20001101	28.99	89.21	
	*AST3A1 001101050017120515 0010	20001101	28.46	89.08	
	*AST3A1 001101050026120515 0003	20001101	27.93	88.95	
	AST3A1 030110044749120515 0031	20030110	28.36	89.83	
	AST3A1 030110044758120515 0030	20030110	27.82	89.70	
	*AST3A1 040301044724150727 0001	20040301	28.95	89.50	
	AST3A1 040301044733120515 0033	20040301	28.42	89.37	
	AST3A1 040301044741120515 0004	20040301	27.89	89.24	
					In total, 380 (Level-3A) 6 (Level-1B) products

[1] The first 6 digits after space in the granule ID denotes the observation date of the ASTER product.

[2] The first 6 digits in the last 10 digits of the granule ID denotes the date of the ASTER data processing.

*Redundant data already listed above.

Peer-reviewed version available at Geosciences 2016, 6, 39; doi:10.3390/geosciences6030039

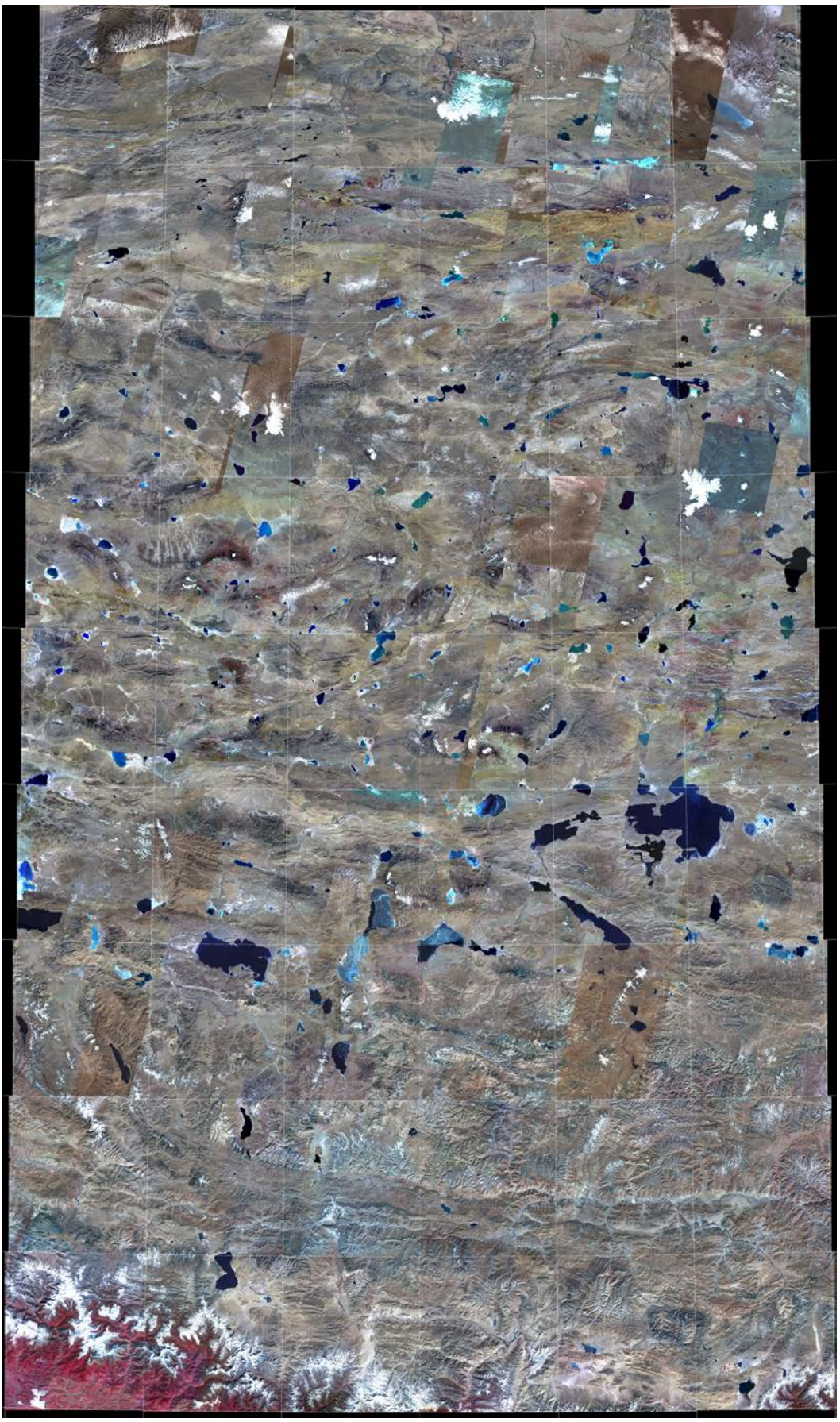

Figure A1. High resolution version of Figure 2 without annotated information.

Peer-reviewed version available at Geosciences 2016, 6, 39; doi:10.3390/geosciences6030039

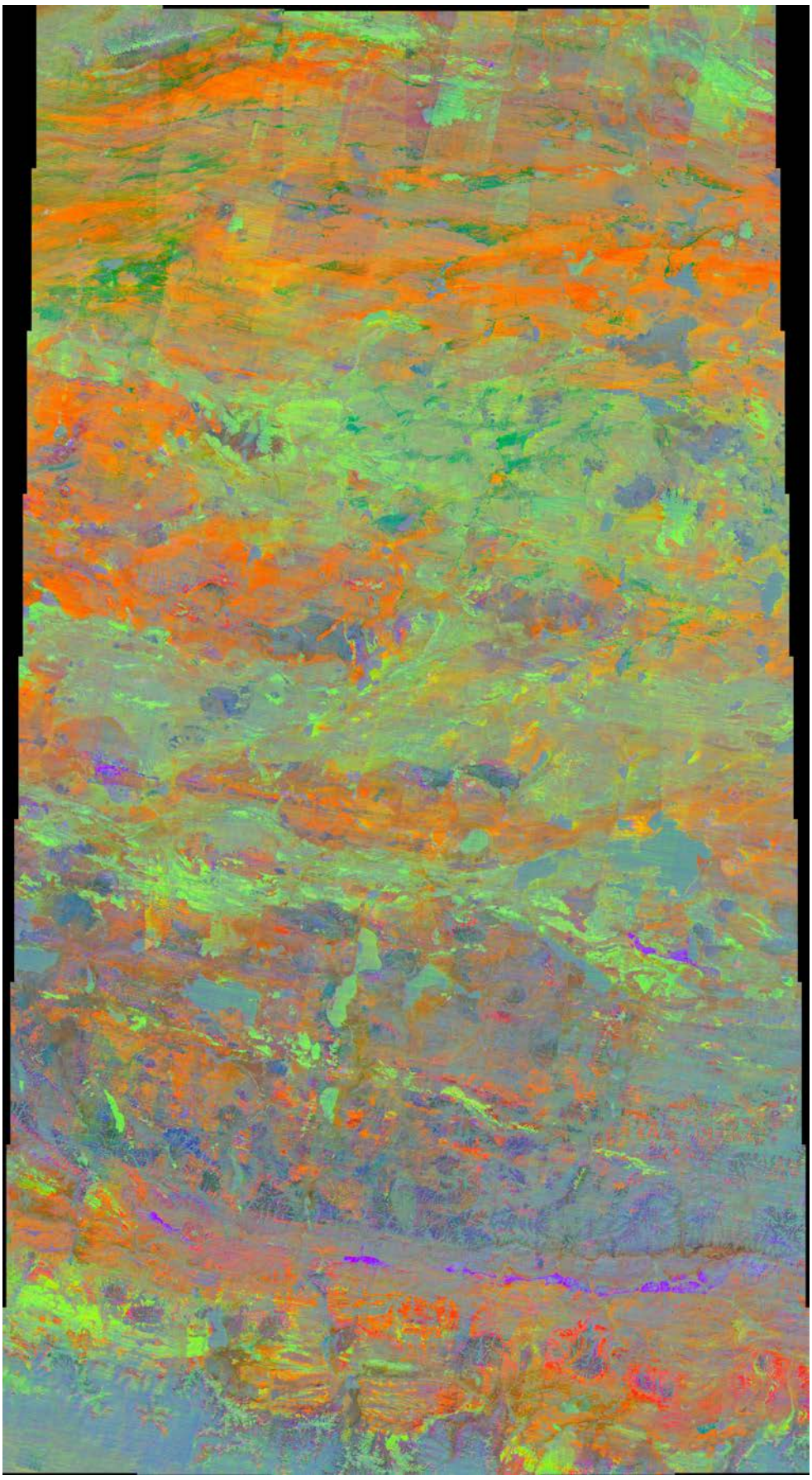

Figure A2. High resolution version of Figure 4 without annotated information.

Peer-reviewed version available at Geosciences 2016, 6, 39; doi:10.3390/geosciences6030039

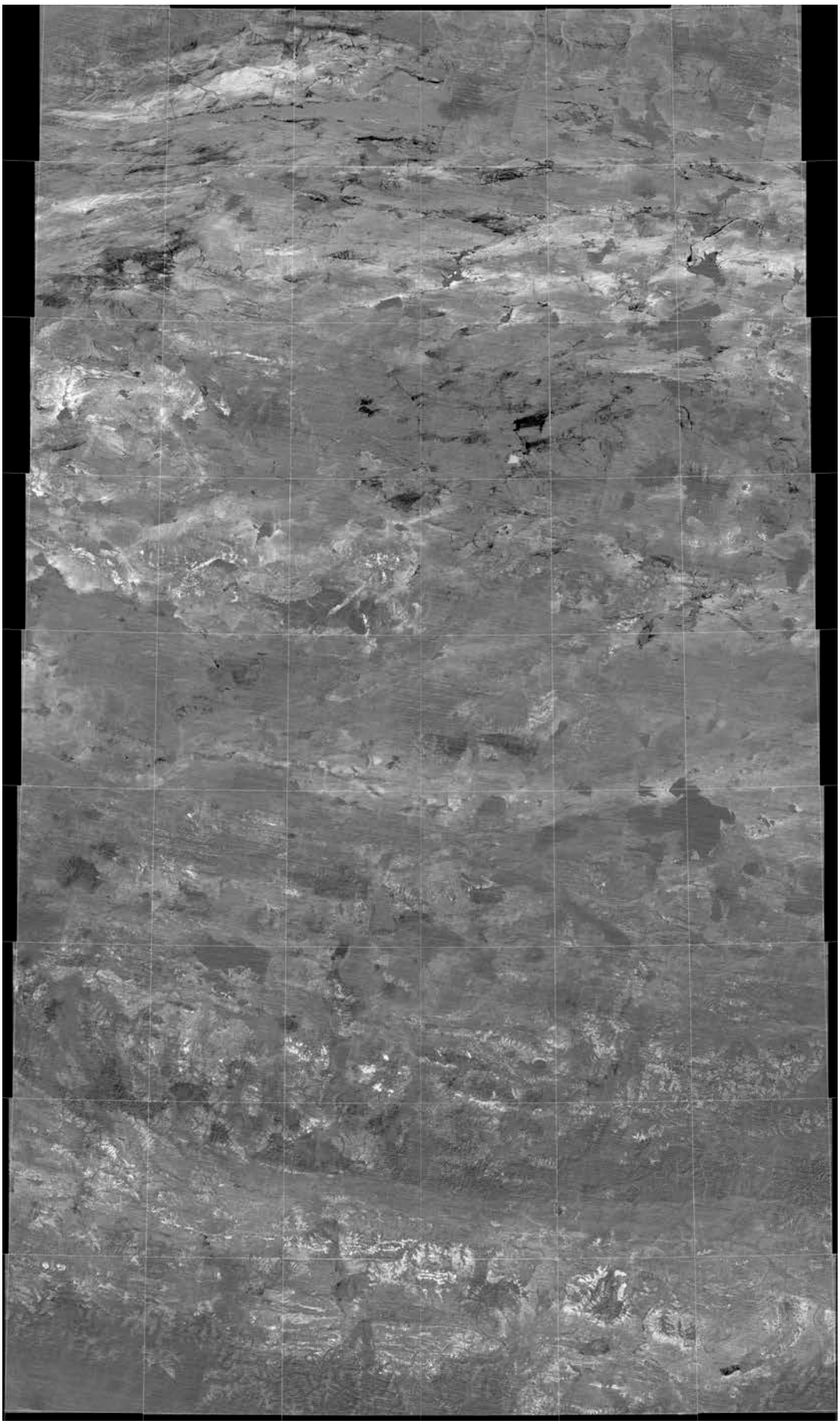

Figure A3. High resolution version of Figure 5 (a) without annotated information.

Peer-reviewed version available at Geosciences 2016, 6, 39; doi:10.3390/geosciences6030039

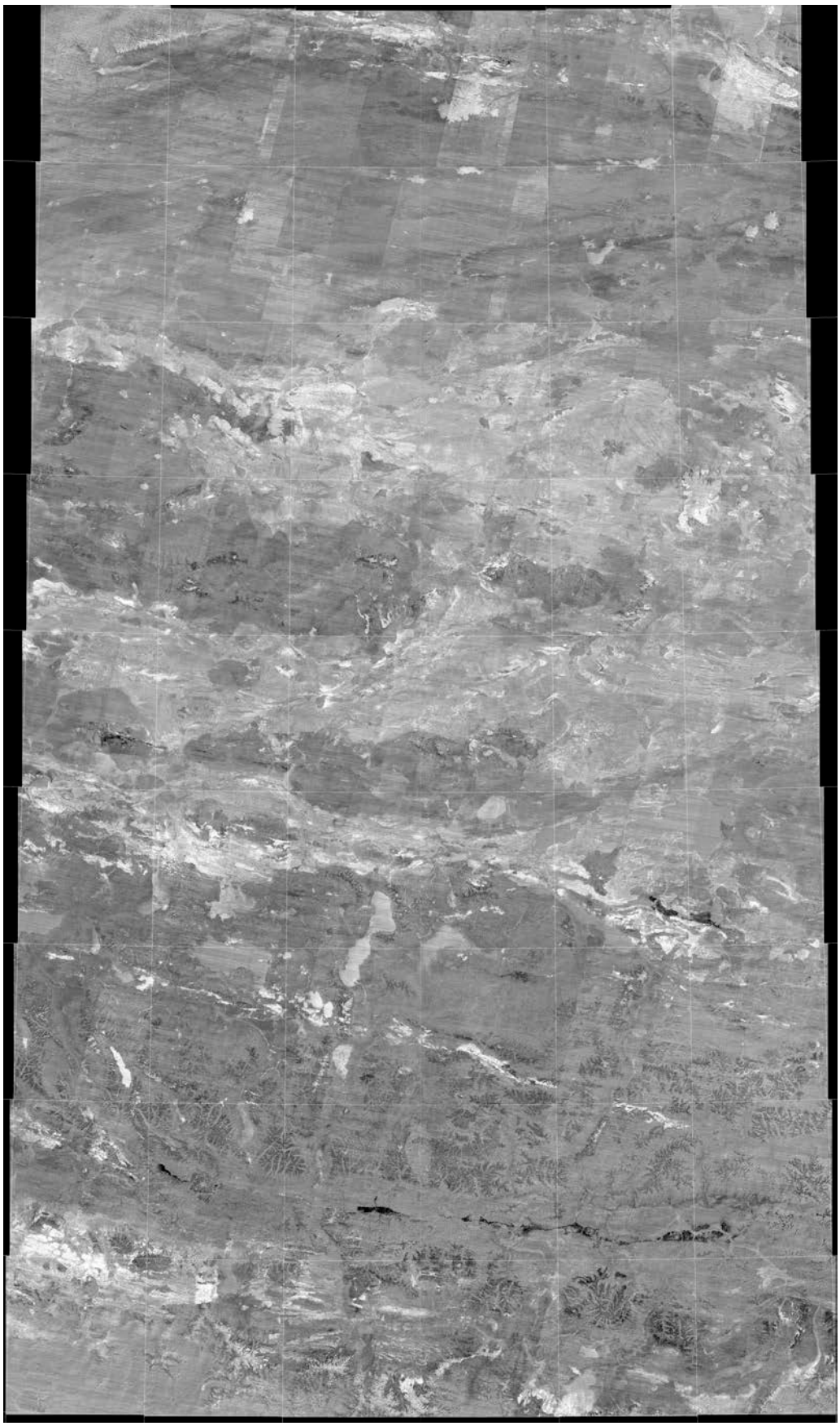

Figure A4. High resolution version of Figure 5 (b) without annotated information.

Figure A5. High resolution version of Figure 5 (c) without annotated information.

Peer-reviewed version available at Geosciences 2016, 6, 39; doi:10.3390/geosciences6030039

Figure A6. High resolution version of Figure 6 without annotated information.

Peer-reviewed version available at Geosciences 2016, 6, 39; doi:10.3390/geosciences6030039

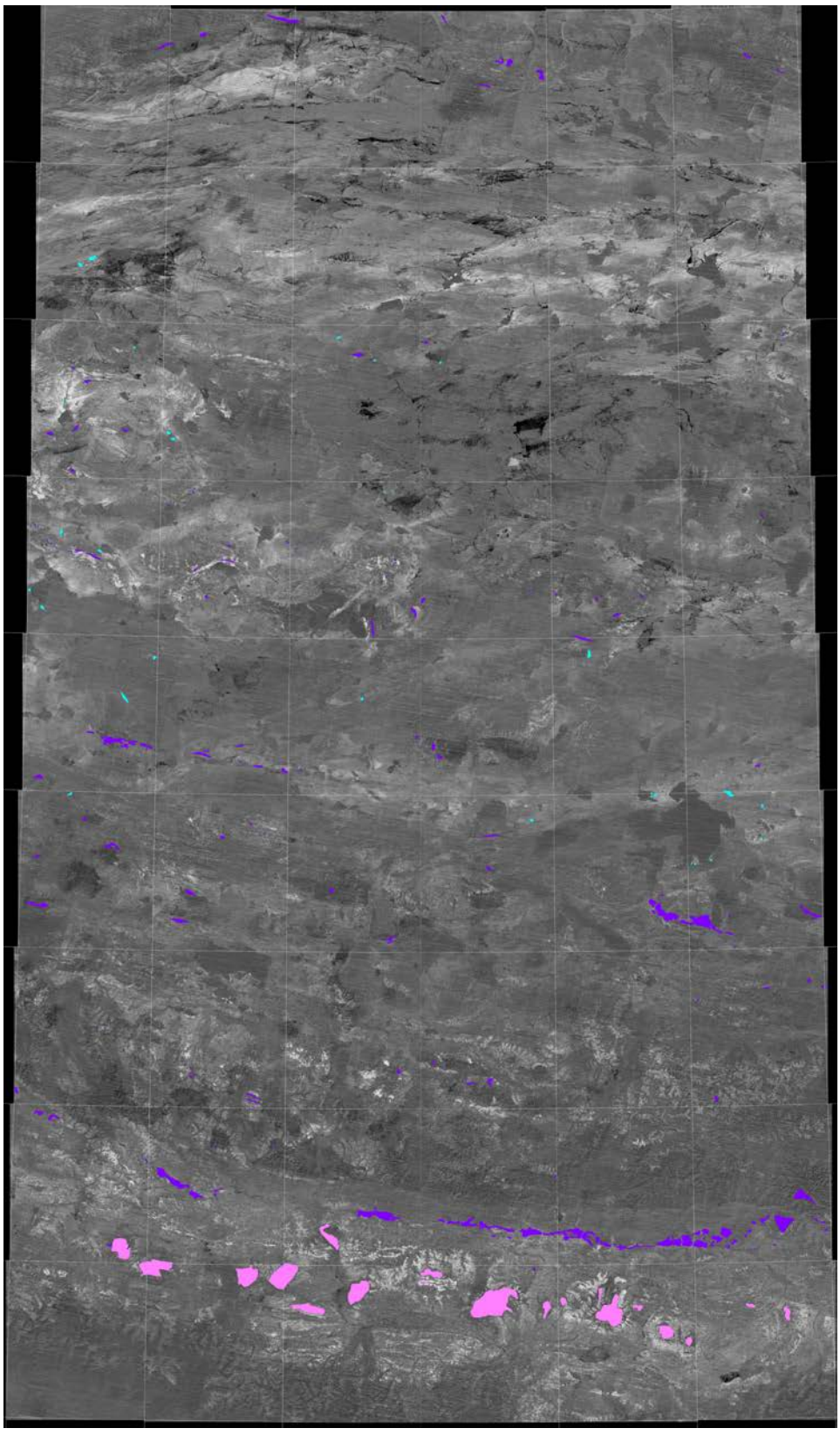

Figure A7. High resolution version of Figure 8 without annotated information.

References

1. Hunt, J.M.; Wisherd, M.P.; Bonham, L.C. Infrared Absorption Spectra of Minerals and Other Inorganic Compounds. *Anal. Chem.*, **1950**, *22*, pp. 1478–1497, DOI: 10.1021/ac60048a006. Available online: http://pubs.acs.org/doi/abs/10.1021/ac60048a006 (accessed on 30 April 2016).
2. Miller, F.A.; Wilkins, C.H. Infrared Spectra and Characteristic Frequencies of Inorganic Ions. *Anal. Chem.*, **1952**, *24*, pp. 1253–1294, DOI: 10.1021/ac60068a007. Available online: http://pubs.acs.org/doi/abs/10.1021/ac60068a007 (accessed on 30 April 2016).
3. Hunt, G.R. Spectral signatures of particulate minerals in visible and near infrared. *Geophy.* **1977**, *42*, pp. 501–513, DOI: 10.1190/1.1440721. Available online: http://geophysics.geoscienceworld.org/content/42/3/501 (accessed on 30 April 2016).
4. Logan, L.M.; Hunt, G.R.; Salisbury, J.W.; Salvatore, R.B. Compositional implications of Christiansen frequency maximums for infrared remote sensing applications. *J. Geophy. Res.* **1973**, *78*, pp. 4983–5003, DOI: 10.1029/JB078i023p04983. Available online: http://onlinelibrary.wiley.com/doi/10.1029/JB078i023p04983/full (accessed on 30 April 2016).
5. Stubican, V.; Roy, R. Infrared Spectra of Layer-Structure Silicates. *J. Amer. Ceramic Soc.* **1961**, *44*, pp. 625–627, DOI: 10.1111/j.1151-2916.1961.tb11670.x. Available online: http://onlinelibrary.wiley.com/doi/10.1111/j.1151-2916.1961.tb11670.x/full (accessed on 30 April 2016).
6. Lyon, R.J.P. *Evaluation of infrared spectrophotometry for compositional analysis of lunar and planetary soils*, Final Rep. PSU–3943; SRI: Menlo Park, CA, USA, **1964**; 278 p.
7. Vincent, R.K.; Thomson, F.J. Rock-Type Discrimination from Ratioed Infrared Scanner Images of Pisgah Crater, California. *Sci.* **1972**, *175*, pp. 986–988, DOI: 10.1126/science.175.4025.986. Available online: http://science.sciencemag.org/content/175/4025/986 (accessed on 30 April 2016).
8. Prabhakara, C.; Dalu, G. Remote sensing of the surface emissivity at 9 μm over the globe. *J. Geophy. Res.* **1976**, *81*, pp. 3719–3724, DOI: 10.1029/JC081i021p03719. Available online: http://onlinelibrary.wiley.com/doi/10.1029/JC081i021p03719/full (accessed on 30 April 2016).
9. Kahle, A.B.; Rowan, L.C. Evaluation of multispectral middle infrared aircraft images for lithologic mapping in the East Tintic Mountains, Utah. *Geol.* **1980**, *8*, pp. 234–239, DOI: 10.1130/0091-7613. Available online: http://geology.gsapubs.org/content/8/5/234.abstract (accessed on 30 April 2016).
10. Kahle, A.B. Surface emittance, temperature, and thermal inertia derived from Thermal Infrared Multispectral Scanner (TIMS) data for Death Valley, California. *Geophy.* **1987**, *52*, pp. 858–874, DOI: 10.1190/1.1442357. Available online: http://library.seg.org/doi/abs/10.1190/1.1442357 (accessed on 30 April 2016).
11. Fu, B.; Chou, X. Thermal infrared spectra and TIMS imagery features of sedimentary rocks in the Kalpin Uplift, Tarim Basin, China. *Geocarto Int.* **1998**, *13*, pp. 69–73, DOI: 10.1080/10106049809354630. Available online: http://www.tandfonline.com/doi/abs/10.1080/10106049809354630 (accessed on 30 April 2016).
12. Yamaguchi, Y.; Kahle, A.B.; Tsu, H.; Kawakami, T.; Pniel, M. Overview of Advanced Spaceborne Thermal Emission and Reflection Radiometer (ASTER). *IEEE Trans. Geosci. Remote Sens.* **1998**, *36*, pp. 1062–1071, DOI: 10.1109/36.700991. Available online: http://ieeexplore.ieee.org/xpl/articleDetails.jsp?arnumber=700991&filter%3DAND%28p_IS_Number%3A15154%29 (accessed on 30 April 2016).
13. Ninomiya, Y.; Fu, B. Quartz index, carbonate index and SiO2 content index defined for ASTER TIR data. *J. Remote Sens. Soc. Japan*. **2002**, *22*, 50–61 (in Japanese with English abstract), DOI: 10.11440/rssj1981.22.50. Available online: https://www.jstage.jst.go.jp/article/rssj1981/22/1/22_1_50/_article/-char/ja/ (accessed on 30 April 2016).
14. Ninomiya, Y. Mapping quartz, carbonate minerals and mafic-ultramafic rocks using remotely sensed multispectral thermal infrared ASTER data. *Proc. of SPIE*. **2002**, *4710*, pp. 191–202, DOI: 10.1117/12.459566. Available online: http://proceedings.spiedigitallibrary.org/proceeding.aspx?articleid=884835 (accessed on 30 April 2016).
15. Ninomiya, Y. Rock type mapping with indices defined for multispectral thermal infrared ASTER data: case studies. *Proc. of SPIE*. **2003**, *4886*, pp. 123–132, DOI: 10.1117/12.462358. Available online: http://proceedings.spiedigitallibrary.org/proceeding.aspx?articleid=880249 (accessed on 30 April 2016).
16. Ninomiya, Y. Lithologic mapping with multispectral ASTER TIR and SWIR data. *Proc. of SPIE*. **2004**, *5234*, pp. 180–190, DOI: 10.1117/12.511902. Available online: http://proceedings.spiedigitallibrary.org/proceeding.aspx?articleid=830186 (accessed on 30 April 2016).

17. Ninomiya, Y.; Fu, B.; Cudahy, T.J. Detecting lithology with Advanced Spaceborne Thermal Emission and Reflection Radiometer (ASTER) multispectral thermal infrared "radiance-at-sensor" data. *Remote Sens. Envir.* **2005**, *99*, 127–139, DOI: 10.1016/j.rse.2005.06.009. Available online: http://www.sciencedirect.com/science/article/pii/S0034425705002142 (accessed on 30 April 2016).
18. Corrie, R.K.; Ninomiya, Y.; Aitchison, J.C. Applying Advanced Spaceborne Thermal Emission and Reflection Radiometer (ASTER) spectral indices for geological mapping and mineral identification on the Tibetan Plateau. *Int. Arch. Photo., Remote Sens., Spatial Info. Sci.* **2010**, *XXXVIII*, 464–469, Available online: http://www.isprs.org/proceedings/xxxviii/part8/pdf/W05P01_20100308025647.pdf (accessed on 30 April 2016).
19. Aboelkhair, H.; Ninomiya, Y.; Watanabe, Y.; Sato, I. Processing and interpretation of ASTER TIR data for mapping of rare-metal-enriched albite granitoids in the Central Eastern Desert of Egypt. *J. African Earth Sci.* **2010**, *58*, 141–151, DOI: 10.1016/j.jafrearsci.2010.01.007. Available online: http://www.sciencedirect.com/science/article/pii/S1464343X10000178 (accessed on 30 April 2016).
20. Khan, S.D.; Mahmood, K. The application of remote sensing techniques to the study of ophiolites. *Earth-Sci. Rev.* **2008**, *89*, pp. 135–143, DOI: 10.1016/j.earscirev.2008.04.004. Available online: http://www.sciencedirect.com/science/article/pii/S0012825208000561 (accessed on 30 April 2016).
21. Mitsuishi, M.; Wallis, S.R.; Aoya, M.; Lee, J.; Wang, Y. E–W extension at 19 Ma in the Kung Co area, S. Tibet: Evidence for contemporaneous E–W and N–S extension in the Himalayan orogen. *Earth and Planetary Sci. Let.* **2012**, *325–326*, 10–20, DOI: 10.1016/j.epsl.2011.11.013. Available online: http://www.sciencedirect.com/science/article/pii/S0012821X11006704 (accessed on 30 April 2016).
22. Guha, A.; Kumar, V. New ASTER derived thermal indices to delineate mineralogy of different granitoids of an Archaean Craton and analysis of their potentials with reference to Ninomiya's indices for delineating quartz and mafic minerals of granitoids—An analysis in Dharwar Craton, India. *Ore Geol. Rev.* **2016**, *74*, 76–87, DOI: 10.1016/j.oregeorev.2015.10.033. Available online: http://www.sciencedirect.com/science/article/pii/S0169136815301724 (accessed on 30 April 2016).
23. Tommaso, I.D.; Rubinstein, N. Hydrothermal alteration mapping using ASTER data in the Infiernillo porphyry deposit, Argentina. *Ore Geol. Rev.* **2007**, *32*, 275–290, DOI:10.1016/j.oregeorev.2006.05.004. Available online: http://www.sciencedirect.com/science/article/pii/S016913680600076X (accessed on 22 June 2016).
24. Rockwell, B.W.; Hofstra, A.H. Identification of quartz and carbonate minerals across northern Nevada using ASTER thermal infrared emissivity data—Implications for geologic mapping and mineral resource investigations in well-studied and frontier areas. *Geosphere.* **2008**, *4*, 218-246, DOI: 10.1130/GES00126.1. Available online: http://geosphere.gsapubs.org/content/4/1/218.full (accessed on 22 June 2016).
25. Rajendran, S.; Hersi, O.S.; Al-Harthy, A.; Al-Wardi, M.; El-Ghali, M.A.; Al-Abri, A.H. Capability of advanced spaceborne thermal emission and reflection radiometer (ASTER) on discrimination of carbonates and associated rocks and mineral identification of eastern mountain region (Saih Hatat window) of Sultanate of Oman. *Carbonates Evaporites.* **2011**, *26*, 351–364, DOI 10.1007/s13146-011-0071-4. Available online: http://link.springer.com/article/10.1007/s13146-011-0071-4 (accessed on 22 June 2016).
26. Ding, C.; Liu, X.; Liu, W.; Liu, M.; Li, Y. Mafic–ultramafic and quartz-rich rock indices deduced from ASTER thermal infrared data using a linear approximation to the Planck function. *Ore Geol. Rev.* **2014**, *60*, 161–173, DOI:10.1016/j.oregeorev.2014.01.005. Available online: http://www.sciencedirect.com/science/article/pii/S0169136814000110 (accessed on 22 June 2016).
27. Pournamdari, M.; Hashim, M. Detection of chromite bearing mineralized zones in Abdasht ophiolite complex using ASTER and ETM$^+$ remote sensing data. *Arab. J. Geosci.* **2014**, *7*, 1973–1983, DOI 10.1007/s12517-013-0927-0. Available online: http://link.springer.com/article/10.1007/s12517-013-0927-0 (accessed on 22 June 2016).
28. Emam, A.; Zoheir, B.; Johnson, P. ASTER-based mapping of ophiolitic rocks: examples from the Allaqi–Heiani suture, SE Egypt. *Int. Geol. Rev.* **2016**, *58*, 525-539, DOI: 10.1080/00206814.2015.1094382. Available online: http://www.tandfonline.com/doi/abs/10.1080/00206814.2015.1094382 (accessed on 22 June 2016).
29. Rajendran, S. Mapping of Neoproterozoic source rocks of the Huqf Supergroup in the Sultanate of Oman using remote sensing. *Ore Geol. Rev.* **2016**, *78*, 281–299, DOI:10.1016/j.oregeorev.2016.03.024. Available online: http://www.sciencedirect.com/science/article/pii/S0169136815301402 (accessed on 22 June 2016).

30. Ninomiya, Y.; Fu, B. Regional scale lithologic mapping in western Tibet using ASTER thermal infrared multispectral data. *Int. Arch. Photo., Remote Sens., Spatial Info. Sci.* **2010**, *XXXVIII*, 454–458, Available online: http://www.isprs.org/proceedings/xxxviii/part8/pdf/W05O04_20100308220541.pdf (accessed on 30 April 2016).
31. Molnar, P.; Tapponnier, P. Cenozoic Tectonics of Asia. *Sci.* **1975**, *189*, pp. 419–426, DOI: 10.1126/science.189.4201.419. Available online: http://science.sciencemag.org/content/189/4201/419 (accessed on 30 April 2016).
32. Dewey, J.F.; Shackleton, R.M.; Chengfa, C.; Yiyin, S. Cenozoic Tectonics of Asia. *Phil. Trans. Royal Soc. London A.* **1988**, *327*, pp. 379–413, DOI: 10.1098/rsta.1988.0135. Available online: http://rsta.royalsocietypublishing.org/content/327/1594/379 (accessed on 30 April 2016).
33. Fu, B.; Walker, R.; Sandiford, M. The 2008 Wenchuan earthquake and active tectonics of Asia. *J. Asian Earth Sci.* **2011**, *40*, 797–805, DOI: 10.1016/j.jseaes.2011.01.003. Available online: http://www.sciencedirect.com/science/article/pii/S1367912011000216 (accessed on 30 April 2016).
34. Pan, G.; Wang, G.; Li, R.; Yuan, S.; Ji, W.; Yin, F.; Zhan, W. Tectonic evolution of the Qinghai-Tibet Plateau. *J. Asian Earth Sci.* **2012**, *54*, 3–14, DOI: 10.1016/j.jseaes.2011.12.018. Available online: http://www.sciencedirect.com/science/article/pii/S1367912012000065 (accessed on 30 April 2016).
35. Xu, Z.; Dilek, Y.; Cao, H.; Yang, J.; Robinson, P.; Ma, C.; Li, H.; Jolivetf, M.; Rogerg, F.; Chena, X. Paleo-Tethyan evolution of Tibet as recorded in the East Cimmerides and West Cathaysides. *J. Asian Earth Sci.* **2015**, *105*, 320–334, DOI: 10.1016/j.jseaes.2015.01.021. Available online: http://www.sciencedirect.com/science/article/pii/S1367912015000498 (accessed on 30 April 2016).
36. Burchfiel, B.C.; Chen, Z.; Hodges, K.V.; Liu, Y.; Royden, L.H.; Deng, C.; Xu, J. *The South Tibetan Detachment System, Himalayan orogen: Extension contemporaneous with and parallel to shortening in a collisional mountain belt*, Special Paper 269; Geol. Soc. Amer., Boulder, Colorado, USA. **1992**; 41 p. DOI: 10.1130/SPE269-p1. Available online: http://specialpapers.gsapubs.org/content/269/1.full.pdf+html (accessed on 22 June 2016).
37. Aoya, M.; Wallis, S.R.; Terada, K.; Lee, J.; Kawakami, T.; Wang, Y.; Heizler, M. North-south extension in the Tibetan crust triggered by granite emplacement. *Geol.* **2005**, *33*, 853–856, DOI: 10.1130/G21806.1. Available online: http://geology.gsapubs.org/content/33/11/853 (accessed on 30 April 2016).
38. Burg, J.P.; Guiraud, M.; Chen, G.M.; Li, G.C. Himalayan metamorphism and deformations in the North Himalayan Belt (southern Tibet, China). *Earth and Planetary Sci. Let.* **1984**, *69*, 391-400, DOI: 10.1016/0012-821X(84)90197-3. Available online: http://www.sciencedirect.com/science/article/pii/0012821X84901973 (accessed on 22 June 2016).
39. Girardeau, J.; Marcoux, J.; Foucade, E.; Bassoullet, J.P.; Tang, Y. Xainxa ultramafic rocks, central Tibet, China: Tectonic environment and geodynamic significance. *Geol.* **1985**, *13*, 330–333, DOI: 10.1130/0091-7613(1985)13<330:XURCTC>2.0.CO;2. Available online: http://geology.gsapubs.org/content/13/5/330.short (accessed on 22 June 2016).
40. Qu, W.G.; Wang, Y.S.; Zhang, S.Q.; Wang, Z.H.; LU, P.; Duan, J.X. New results and major progress in regional geological survey of the Toiba district sheet (1:250,000). *Geol. Bulletin China*. **2004**, *23*, 492-497 (in Chinese with English abstract).
41. Wang, W.L.; Aitchison, J.C.; Lo, C.H.; Zeng, Q.G. Geochemistry and geochronology of the amphibolite blocks in ophiolitic mélanges along Bangong-Nujiang suture, central Tibet. J. Asian Earth Sci. 2008, 33, 122–138, DOI: 10.1016/j.jseaes.2007.10.022. Available online: http://www.sciencedirect.com/science/article/pii/S1367912007002155 (accessed on 22 June 2016).
42. Baxter, A.T.; Aitchison, J.C.; Zyabrev, S.V. Radiolarian age constraints on Mesotethyan ocean evolution, and their implications for development of the Bangong–Nujiang suture, Tibet. *J. Geol. Soc.* **2009**, *166*, 689–694, DOI: 10.1144/0016-76492008-128. Available online: http://jgs.lyellcollection.org/content/166/4/689 (accessed on 30 April 2016).
43. Zhai, Q.; Jahn, B.; Wang, J.; Su, L.; Mo, X.; Wang, K.; Tang, S.; Lee, H. The Carboniferous ophiolite in the middle of the Qiangtang terrane, Northern Tibet: SHRIMP U–Pb dating, geochemical and Sr–Nd–Hf isotopic characteristics. *Lithos*. **2013**, *168-169*, 186-199, DOI: 10.1016/j.lithos.2013.02.005. Available online: http://www.sciencedirect.com/science/article/pii/S0024493713000376 (accessed on 22 June 2016).
44. Chengdu Institute of Geology and Mineral Resources, Chinese Academy of Geological Sciences, *Geological Map of Qinghai-Tibetan Plateau.* Geological Publishing House, Beijing, China. **1988**.

45. Wang, X., Xiao, X., Cao, Y., Zheng, H., *Geological map of the ophiolite zone along the middle Yarlung Zangbo (Tsangpo) river, Xizang (Tibet)*, Publishing House of Surveying and Mapping, Beijing, China. **1984**.
46. ASTER Global Digital Elevation Model (GDEM). Available online: http://www.jspacesystems.or.jp/ersdac/GDEM/E/index.html (accessed on 30 April 2016).
47. NASA, Japan Make ASTER Earth Data Available At No Cost. Available online: http://www.nasa.gov/feature/jpl/nasa-japan-make-aster-earth-data-available-at-no-cost (accessed on 30 April 2016).
48. Earth Remote Sensing Data Analysis Center. ASTER Reference Guide, Version 1.0. 2003; 47 p. Available online: https://unit.aist.go.jp/igg/rs-rg/ASTERSciWeb_AIST/en/documnts/refernce.html (accessed on 30 April 2016).
49. Earth Remote Sensing Data Analysis Center. ASTER User's Guide Part I General, Version 4.0. 2005; 100 p. Available online: https://unit.aist.go.jp/igg/rs-rg/ASTERSciWeb_AIST/en/documnts/users_guide/index.html (accessed on 30 April 2016).
50. Earth Remote Sensing Data Analysis Center. ASTER User's Guide Part II Level 1 Data Products, Version 5.1. 2007; 66 p. Available online: https://unit.aist.go.jp/igg/rs-rg/ASTERSciWeb_AIST/en/documnts/users_guide/index.html (accessed on 30 April 2016).
51. Level-1 Data Working Group, ASTER Science Team, Japan. Algorithm Theoretical Basis Document for ASTER Level-1 Data Processing, Version 3.0. 1996; 117 p. Available online: https://unit.aist.go.jp/igg/rs-rg/ASTERSciWeb_AIST/en/documnts/atbd.html (accessed on 30 April 2016).
52. Thome, K.; Biggar, S.; Takashima, T. Algorithm Theoretical Basis Document for ASTER Level 2B1 - Surface Radiance and ASTER Level 2B5 - Surface Reflectance. 1999; 45 p. Available online: https://unit.aist.go.jp/igg/rs-rg/ASTERSciWeb_AIST/en/documnts/atbd.html (accessed on 30 April 2016).
53. Palluconi, F.; Hoover, G.; Alley, R.; Jentoft-Nilsen, M.; Thompson, T. An Atmospheric Correction Method for ASTER Thermal Radiometry over Land, Revision 3. 1999; 27 p. Available online: https://unit.aist.go.jp/igg/rs-rg/ASTERSciWeb_AIST/en/documnts/atbd.html (accessed on 30 April 2016).
54. Gillespie, A.R.; Rokugawa, S.; Hook, S.J.; Matsunaga, T.; Kahle, A.B. Temperature/Emissivity Separation Algorithm Theoretical Basis Document, Version 2.4. 1999; 64 p. Available online: https://unit.aist.go.jp/igg/rs-rg/ASTERSciWeb_AIST/en/documnts/atbd.html (accessed on 30 April 2016).
55. Earth Remote Sensing Data Analysis Center. ASTER User's Guide Part III DEM Product (L4A01), Version 1.1. 2005; 19 p. Available online: https://unit.aist.go.jp/igg/rs-rg/ASTERSciWeb_AIST/en/documnts/users_guide/index.html (accessed on 30 April 2016).
56. Earth Remote Sensing Data Analysis Center. ASTER User's Guide Part III 3D Ortho Product (L3A01), Version 1.1. 2004; 18 p. Available online: https://unit.aist.go.jp/igg/rs-rg/ASTERSciWeb_AIST/en/documnts/users_guide/index.html (accessed on 30 April 2016).
57. METI AIST Data Archive System (MADAS). Available online: https://gbank.gsj.jp/madas/?lang=en#top (accessed on 30 April 2016).
58. ASTER Overview, Land Processes Distributed Active Archive center (LP DAAC), USGS. Available online: https://lpdaac.usgs.gov/dataset_discovery/aster (accessed on 30 April 2016).